Journal of Hydrology 607 (2022) 127516

Contents lists available at ScienceDirect

Journal of Hydrology

journal homepage: www.elsevier.com/locate/jhydrol

Research papers

Investigation on the unsteady-state two-phase fluid transport in the nano-pore system of natural tight porous media

Juncheng Qiao [a,b,c,*], Jianhui Zeng [a,b,*], Shu Jiang [c], Guangqing Yang [a,b], Yongchao Zhang [d], Xiao Feng [e], Sen Feng [a,b]

[a] State Key Laboratory of Petroleum Resources and Prospecting, China University of Petroleum, Beijing 102249, China
[b] College of Geosciences, China University of Petroleum, Beijing 102249, China
[c] Key Laboratory of Tectonics and Petroleum Resources of Ministry of Education, School of Earth Resources, China University of Geosciences, Wuhan 430074, China
[d] The Key Laboratory of Gas Hydrate, Ministry of Natural Resources, Institute of Marine Geology, Qingdao 266071, China
[e] CNPC Engineering Technology R&D Company Limited, Beijing 102206, China

ARTICLE INFO

This manuscript was handled by Huaming Guo, Editor-in-Chief

Keywords:
Primary gas intrusion
Unsteady-state two-phase fluid transport
Micro-nanometer pore system
Fluid mobility potential
Dynamic gas accessibility
Tight porous sandstone

ABSTRACT

Fluid transport across the natural tight micro-nanometer porous media governs numerous subsurface geological and industrial activities. The unsteady-state two-phase fluid flow at the very initial stage of non-wetting phase fluid intrusion, governing the hydrocarbon accumulation and CO_2 geological sequestration process, remains uncertain. A modified unsteady-state pressurization gas displacement experiment incorporating systematic pore structure description combining mercury porosimetry, nuclear magnetic resonance, and X-ray computed tomography is conducted on the tight sandstone cores to investigate the fluid flow behaviors and to uncover their pore-scale controls. The results indicate that the unsteady-state gas–water flow deviates from Darcy's law, in which the threshold for the onset of continuous non-wetting phase fluid intrusion (ISTP) can be observed and degree of water movement and gas intrusion strongly depend on the injection pressure. Analyses under circular pore assumption, water layer distribution model based on DLVO theory, effective flow assumption, and overall pore connectivity evaluation suggest that the water movement and gas accessibility increases are dominated by the water displacement in the free water layer zone when injection pressure $<$ ISTP, while the criticality of continuous gas intrusion is determined by the water movement in the inner layer of weakly bound water zone located in the narrow parts of the connected pathways, especially that in the pores $<$ 40 nm, but its increment mainly occurs in the out layer of the weakly bound water zone when injection pressure $>$ ISTP. Distinctions in the distributions and proportions of free and bound water layers in the different connected pore systems lead to the significant variations in the ISTP, water mobility, and gas accessibility of tight sandstone. The primary reasons for the differences in the static fluid mobility and flow behaviors lay in the differed structural attributes of connected pore systems. The narrowing, heterogeneity increase, and actual flow length increment of the connected pathways will raise the resistance for continuous non-wetting phase flow and lead to losses in water mobility, accessibility of non-wetting phase fluid, and flow velocity in the unsteady-state two-phase fluid flow. The high sensitivity of the dynamic fluid flow and gas accessibility to tortuosity of the connected pore system suggests the unsteady-state two-phase fluid flow behaviors are under the coupled control of pore size, complexity, and heterogeneity.

1. Introduction

Numerous underground geological and industrial processes, e.g. the hydrocarbon accumulation and development, CO_2 geologic sequestration, geothermal extraction, and contaminant pollution control, are governed by the fluid transport through the natural porous media (Bachu, 2000; Bickle, 2009; Blunt, 2017; Spurin et al., 2020). Tight sandstone, an emerging natural reservoir for the hydrocarbon, CO_2, and geothermal energy, attracts research attentions (Thomas and Ward, 1972; Tischner et al., 2010). Understanding the fluid flow mechanism in the tight porous sandstone has direct implications for the resource-related or environmental activities (Bultreys et al., 2016). Studies on

* Corresponding authors at: State Key Laboratory of Petroleum Resources and Prospecting, China University of Petroleum, Beijing 102249, China.
E-mail addresses: Juncheng.Qiao@cup.edu.cn (J. Qiao), zengjh@cup.edu.cn (J. Zeng).

https://doi.org/10.1016/j.jhydrol.2022.127516
Received 2 December 2021; Received in revised form 16 January 2022; Accepted 19 January 2022
Available online 25 January 2022
0022-1694/© 2022 Elsevier B.V. All rights reserved.

fluid transport phenomenon in the low-permeable natural porous media can be dated back to the 1950 s since the publication of Darcy's law in 1856 (Darcy, 1856). An exponential function of single-phase water flow in tight soil was discovered by Swartzendruber (1962a, 1962b). Miller and Low (1963) also found deviations of water seepage from Darcy's law in low-permeability porous media, which had been reported as non-Darcy flow by Prada and Civan (1999) through their sand pack experiments. This was further confirmed by Wang et al. (2015) and Wang and Sheng (2017) using a micro-flux measuring instrument. Dejam et al. (2017a) firstly discussed the Pre-Darcy flow in the shale formations in terms of the power-law model proposed by Hansbo (2001). Farmani et al. (2018) reported the significance of departure from linearity at low fluid velocity (Pre-Darcy flow) in the tight porous media. Zeng et al. (2010) have also confirmed this deviation in the steady-state single-phase oil displacement in tight sandstone cores. Accordingly, the fluid flow in natural tight porous rocks no longer follows the Darcy's law and is known as Pre-Darcy flow at low fluid velocity and non-Darcy flow at high velocity (Kutílek, 1972; Soni et al., 1978; Kececioglu and Jiang, 1994).

The Pre-Darcy flow in the tight porous rocks, characterized by concave-up non-linear flow curves with threshold pressure gradients (TPG) and pseudo threshold pressure gradients (PTPG), involving in plenty of managements and designs of subsurface processes, has been brought to the forefront of current research (Gavin, 2004; Pertsin and Grunze, 2004; Dejam et al., 2017a, b; Farmani et al., 2018). However, the low-velocity Pre-Darcy flow behavior is obtained from the steady-state single-phase flow measurements and therefore can be hardly used to describe the low-velocity unsteady-state two-phase fluid flow (UTFF) that actually involved in the primary fluid charging or intrusion, initial displacement stage of energy resource development, primary leakage in contaminant pollution control, and beginning of the CO_2 geological sequestration (Gavin, 2004; Dukhan et al., 2014; Kundu et al., 2016; Dejam et al., 2017b). Recently, the physics governing the multi-phase flow in natural porous media have been studied by pore-scale displacement experiments, but those in tight porous rocks are poorly understood (Berg et al., 2013; Blunt, 2017; Singh et al., 2017; Spurin et al., 2020). Moreover, the validation of the steady-state multiphase flow mechanisms in the unsteady or transient procedures stays unclear, especially for the Haines jumps, snap-off, or non-wetting phase entrapment phenomenon (Haines, 1930; Berg et al., 2013; Singh et al., 2017). The fluid flow behaviors for the UTFF remain to be investigated, particularly, the onsets of the continuous movement of the saturated wetting phase under the displacement of the other non-wetting phase are rarely reported. It should be clarified that the onsets of continuous two-phase fluid movement under the unsteady-state conditions should not be confused with PTPG or TPG involving in the steady-state single-phase fluid flow or even the breakthrough pressure in the steady-state two-phase flow (Pascal, 1981; Prada and Civan, 1999; Dou et al., 2014; Wang and Sheng, 2017; Wu et al., 2017a). Appropriate fluid flow regime characterizations come first in the investigation of UTFF. The correlation between the Reynolds number (Re) and friction coefficient (F) is sensitive to flow transitions, which has been employed to determine the onsets of Pre-Darcy flow and transitions from linear flow to non-Darcy flowin literatures (Zeng and Grigg, 2006; Bağcı et al., 2014; Kundu et al., 2016; Muljadi et al., 2016). Besides, the single-phase fluid apparent permeability and its relations to the Darcy's permeability have been introduced to characterize the onset of non-Darcy flow in tight porous media (Muljadi et al., 2016). The Re versus F and single-phase fluid apparent permeability could also be further provided and conducted in the UTFF.

Prevailing pores-scale fluid flow investigations have reported that the macroscopic flow properties of the porous media are controlled by the pore-scale fluid flow mechanism, meaning the fluid flow behavior is closely related to the microstructure attributes of the porous media (Tallakstad et al., 2009a, 2009b; Armstrong et al., 2016; Blunt, 2017; Spurin et al., 2020). Recent studies have indicated that the intricate pore structures in micro-nanometer scale are responsible for the non-linear flow phenomenon and presences of evident PTPG and TPG in the tight sandstone or shale. Wu et al. (2017b) found new fluid transport phenomenon, including the dramatically enhanced or decreased water flow rates, in nanochannels with varied hydrophilicity. Zou et al. (2017) and Xia et al. (2017) have discovered that the non-Darcy flow in fractured tight rocks has a strong dependence on the attributes of the void spaces and fracture surface roughness, which agree well with the study of Chen et al. (2019). Muljadi et al. (2016) investigated the effect of pore-scale heterogeneity on non-Darcy flow by means of numerical simulations on a beadpack, Bentheimer sandstone, and Estaillades carbonate, suggesting that the pore heterogeneity accounts for the early transition away from Darcy linearity in tight porous rocks. Qiao et al. (2019) reported that the pore-throat configurations of the tight sandstone strongly affect the two-phase non-linear flow regimes in the natural gas charging process. Some scholars investigated the effects of microstructure of tight porous rocks on the fluid flow in terms of fluid mobility, including fluid saturation, movable water ratio, and fluid occurrence state. Liu et al. (2021) have discovered the strong correlation between the movable oil films and pore size by conducting X-ray computed tomography (X-μCT) scanning on the microfluidic chips. Hui et al. (2020) have further indicated that the movable fluid saturation of tight sandstone is primary influenced by the pore-throat radii. Yang and Yu (2020) suggested the water movability of shale is determined by pore diameters and the minor pores within the predominant pathways filled by weakly bound water are responsible for the presence of TPG. Qiao et al. (2020b) indicated the fluid flow capacity of tight sandstone is determined by the movable porosity contribution from intergranular pores. The understandings for the effects of pore structures on the fluid flow in tight porous sandstone are somehow limited. One of the reasons lies in the difficulties in the systematic pore system description, which can be attributed to the inherent deficiencies of single technique (e.g., mercury intrusion, scanning electron microscope, X-μCT, and nuclear magnetic resonance (NMR)) in measuring the overall pore structures, the other reason lies in the short of investigations on the UTFF phenomenon (Ramstad et al., 2010).

In this paper, we conducted an unsteady-state two-phase fluid flow experiment on the core flooding instruments, in which the wetting-phase water in the cores is displaced by non-wetting gas in order to simulate the initial charging process of natural gas into the tight porous sandstone or primary invasion procedure of CO_2 into the tight seal, to examine the UTFF phenomenon, and to measure its critical features. By conducting the integrated NMR, pressure-controlled mercury intrusion (PCP), and X-μCT on the same cores, we are able to obtain an overall pore structure description of tight sandstone. Coupling analyses of the results enable us to uncovering the underlying physics of, and effects of pore structure on, the unsteady-state multiphase flow in tight porous sandstone. This work tries to enlighten the understandings for the unsteady-state multiphase fluid flow in natural tight porous media, and may provide useful insights for the basin-scale hydrocarbon accumulation, hydrogeological circulation, water–rock interaction, CO_2 geological sequestration, and contaminant pollution control in the tight rocks.

2. Samples and experiments

2.1. Samples

Nine tight sandstone samples were collected from the Permian Shanxi formation at depths of 2300–2800 m in the northeastern Ordos Basin, China. The basin is the one of the most petroliferous interior basins in China, of which the thick fluvial and deltaic feldspathic litharenites and litharenites in the Permian unit exhibit great hydrocarbon storage potentials and good development prospects (Dai et al., 2005; Xiao et al., 2005; Yang et al., 2005). Exploring the UTFF behaviors and their pore-scale controlling factors are of great significance for the understanding of the basin-scale hydrocarbon accumulation,

hydrogeological circulation, and water–rock interactions. It will also provide a guidance for the tight gas recovery enhancement, which may enlighten the associated works in the CO_2 geological sequestration and contaminant pollution control in shale and mudstone.

The nine cylindrical samples with lengths of 40–60 mm and diameters of 25 mm were drilled perpendicular to the bedding planes of the tight sandstone layers and consistent with the natural gas invasion orientation. The helium porosity and Klinkenberg-corrected permeability were examined by the Core Lab apparatus CMS-300 in the state key laboratory of China University of Petroleum Beijing (CUPB) in accordance with the standard SY/T 5336-2006 of China (Qiao et al., 2021). The labels and detailed information of these samples are listed in Table 1.

2.2. Experiments

2.2.1. Unsteady-state gas-water flow experiment

The unsteady-state gas-water flow experiment, of which the saturated wetting-phase water is displaced by non-wetting gas, is performed on the core flooding system (CFS). The CFS is composed of a fluid injection system with controlled injection pressure of 0.02–70.00 MPa, a core holder system with maximum confining pressure of 70.00 MPa, a thermostat system with temperature between 20 and 120 °C, a fluid metering system with accuracies of 0.001 ml/min for liquid and 0.01 ml/min for gas, and an auto data acquisition system controlled by microcomputer (Fig. 1). The gas soap bubble flow meter in the outlet is replaced by a capillary flow meter in order to capture the low water flow rate at the very initial stage. Two pressure transducers are plugged into the upstream and downstream of the core holder to record the pressures during the flow procedures. The confining pressure is at least 2 MPa higher than the injection pressure to eliminate the fracturing risk and gas leakage through the gap between the rubber sleeve and sample.

Prior to the experiments, the air in the cores was evacuated by a vacuum pump before they were saturated with $CaCl_2$ brine solution with salinity of 50000 mg/L that is consistent with the actual formation water condition in the Permian Shanxi Formation. The pipelines were vacuumed and were then injected with the $CaCl_2$ solution for 24 h before the saturated samples were placed into the core holder. The brine solution injection continued for several days to remove the residual air in the system. A stepping pressurization method was employed in the unsteady-state gas–water two-phase flow experiment. Nitrogen was injected into the core with a minimum pressure (~0.02 MPa) with downstream open to the atmosphere. The injection pressure was increased with a step size of 0.02 MPa with each pressure set-point being kept for at about 1–2 h. The pressure and water flow rate Q were recorded since the beginning. The experiment ceased when gas bubbles emerged from the outlet.

2.2.2. Integrated pore structure characterization

Before commencing the integrated pore structure characterization that includes the X-μCT, NMR, and PCP, the samples that have underwent the fluid flow experiments were soaked in the deionized water to remove the residual brine and were then dried for 48 h in the drying oven at the temperature of 80 °C. X-μCT scanning, with a resolution of 3.0 μm, a voxel of 30 mm × 30 mm × 30 mm, a voltage of 90 Kv, a working power of 8 W, and an exposure time of 1000 ms, was firstly conducted on the pretreated samples using a Zeiss Xradia Versa 510 instrument. The pore attributes were derived from the scanning slices that were processed following the processing methodology presented by Qiao et al. (2020a, b, 2021) and Dong and Blunt (2009).

Non-destructive NMR followed the scanning and was conducted on the Numag MicroMR12-025 V NMR spectrometer with a resonance frequency of 11.85 MHz. The test had an echo time of 0.15 ms, waiting time of 2000 ms, echo number of 5000, and scanning times of 32. Two times of NMR measurements were conducted before and after centrifugation (one-hour centrifugation with centrifugal pressure 300 psi) under a temperature of 20 °C. The saturated T_2 spectrum and its correlation with centrifuged T_2 spectrum provide pore structure information, however, the conversion of T_2 to pore size inevitably depends on the determination of the surface relaxation ratio (ρ), which must rely on other techniques.

PCP was performed on the AutoPore IV 9500 analyzer produced by Micromeritics Instrument Corporation. The measurements with highest intrusion pressure of 60,000 psi were performed on the same specimens that have underwent the X-μCT and NMR examinations. The mercury continuously intruded into smaller pore spaces with increasing injection pressure. Once the injection pressure reached maximum, the pressure would gradually decrease, the mercury extrusion occurred simultaneously. The mercury intrusion curves can be converted to pore size distribution using the capillary model.

The integration of X-μCT, NMR, and PCP enables us to the probe the overall pore structure of the tight sandstone. The detailed processing methodology will be introduced in the later section.

3. Results and discussions

3.1. The UTFF behavior

3.1.1. UTFF phenomenon

The specialty of the designed unsteady-state two-phase fluid flow experiment in this investigation lies in the absence of gas flow in the downstream and therefore flow behaviors can only be described by water flow. Differential pressure between the upstream and downstream (ΔP) and water flow rate Q are plotted together with experimental time in Fig. 2. In Fig. 2, the fluid flow can be divided into two stages according to the sectional variation of Q with increasing time and ΔP. In the first stage, no continuous gas or water flow occurs inside the cores since Q is zero at most of time, exhibiting a parallel line close to X axis with little fluctuations. The fluctuations in this stage suggest an intermitted water flow from the downstream, which is attributed to the displacement of part of free water along with the primary gas intrusion under a small pressure gradient. This phenomenon also indicates a discontinuous

Table 1
Sample information.

Sample	Depth, m	Formation	φ, %	K, mD	Q, %	F, %	Ca, %	Do, %	Cl,c%	Py, %	Clay, %				
											S	Ka	C	I	I/S
1#	2642.58	Shanxi, Permian	3.222	0.312	84	/	2	/	14	/	/	32	24	26	18
3#	2690.90	Shanxi, Permian	1.842	0.088	65	/	/	/	35	/	/	26	16	28	30
6#	2578.53	Shanxi, Permian	13.044	0.820	83	/	1	/	16	/	/	16	55	21	8
8#	2751.60	Shanxi, Permian	1.050	0.041	68	/	/	/	32	/	/	27	19	26	28
12#	2433.86	Shanxi, Permian	4.487	1.966	57	/	26	/	17	/	/	18	57	18	7
15#	2584.00	Shanxi, Permian	4.645	0.343	80	/	1	/	18	1	/	16	61	17	6
19#	2691.20	Shanxi, Permian	1.461	0.074	61	/	4	11	23	1	/	24	14	38	24
25#	2347.30	Shanxi, Permian	0.106	0.012	67	/	/	/	31	2	/	27	19	26	28
26#	2768.20	Shanxi, Permian	7.048	0.135	81	/	/	/	19	/	/	27	48	14	11

Note that Q = quartz, F = feldspar, Ca = calcite, Do = Dolomite, Cl = clay, Py = pyrites, S = smectite, Ka = kaolinite, C = chlorite, I = illite, I/S = illite/smectite.

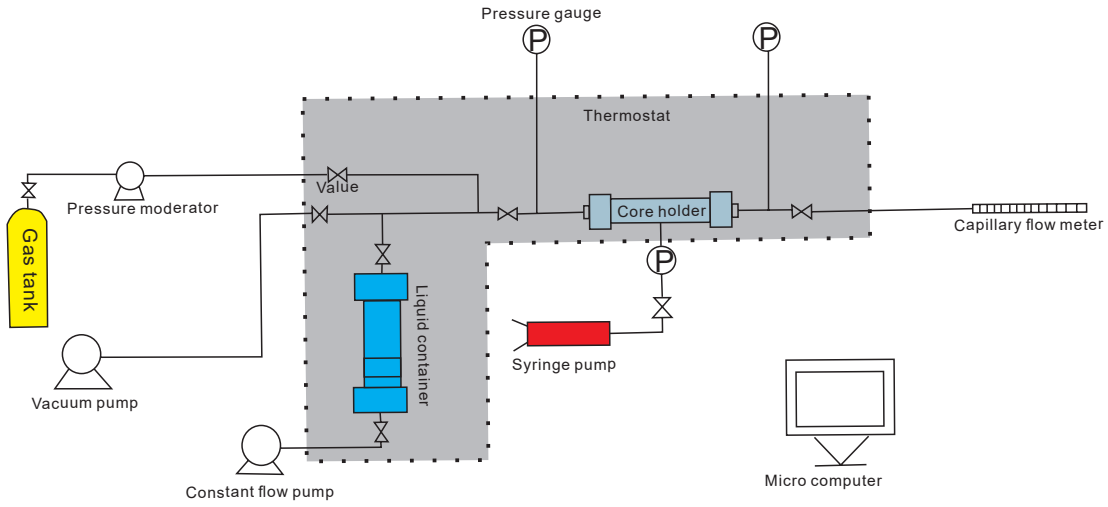

Fig. 1. Core flooding apparatus for the UTFF experiment.

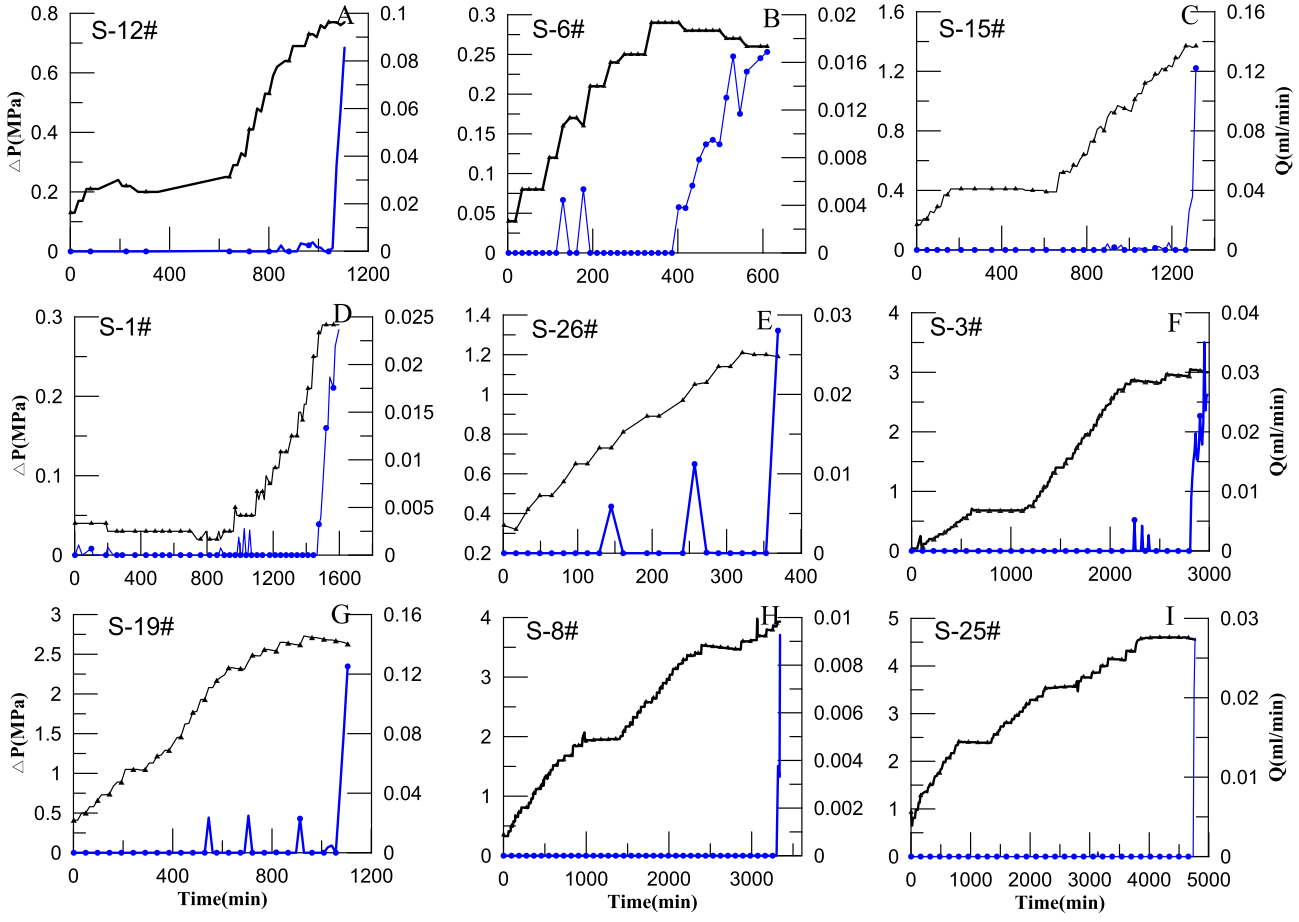

Fig. 2. Plots of time vs. differential gas injection pressure (△P) vs. water flow rate (Q) obtained from the UTFF experiment.

intermitted two-phase flow state in the very initial procedure. In the later stage, a continuous water flow presents, where Q increases with ΔP and time rapidly, exhibiting a quasi-linear flow curve with low-amplitude fluctuations (Haines jumps). It indicates a continuous gas intrusion into the cores. The inflection points between the two stages suggest flow transitions from intermitted discontinuous UTFF to continuous two-phase fluid flow inside the cores, indicating the existences of criticalities for the formation of continuous UTFF in the primary non-wetting phase fluid intrusion procedure. With decreasing permeability, the early-stage fluctuations of Q almost disappear, the curve slopes in the later stage become greater, and the transition points shift to the right on time-axis, meaning increases in sealing capability and reductions in accumulation capacity of tight sandstone. The low-velocity UTFF behaviors are analogues to the low-velocity single-phase Pre-Darcy flow in the tight clays and shale (Fig. 3), in which a threshold pressure for the start-up of the continuous gas intrusion

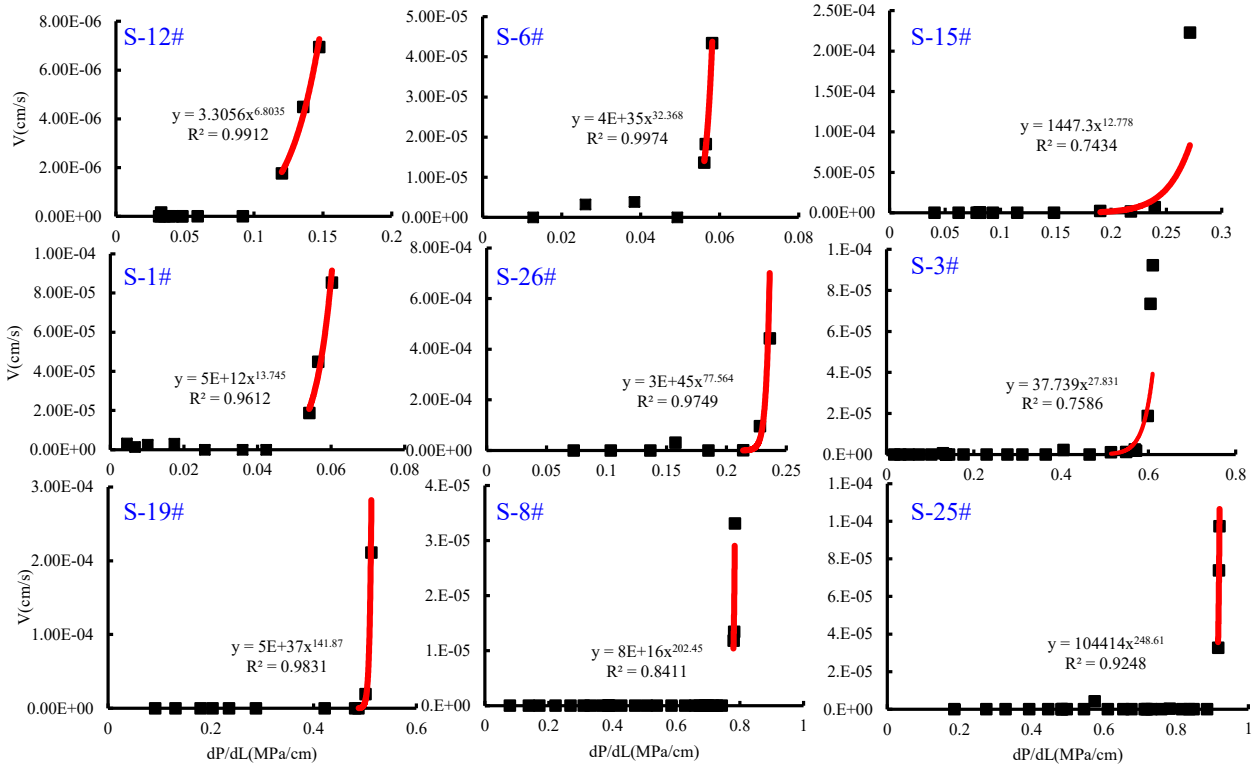

Fig. 3. Plots of water flow velocity (V) vs. differential injection pressure gradient (dP/dL) describing the water seepage behavior in the UTFF procedures (Note that the y in the fitting functions means water flow velocity, V, and x represents pressure gradient, dP/dL).

(ISTP), namely, the criticality for the transitions of non-wetting phase fluid flow from discontinuous to continuous states, can be identified. According to the relationships and fitting correlations between fluid velocity and pressure gradient in Fig. 3, the water flow can be described using the following equations, which drew on the linear and power-law relations between fluid velocity and pressure gradient developed in the Pre-Darcy flow (Puzyrevskaya, 1931; Slepicka, 1961; Siddiqui et al., 2016; Dejam et al., 2017b;).

$$v = \begin{cases} 0 & if \quad \frac{dP}{dL} \le \frac{dP_0}{dL} \\ a\left(\frac{dP}{dL}\right)^m & if \quad \frac{dP}{dL} \ge \frac{dP_0}{dL} \end{cases} \tag{1}$$

where v is the water velocity, cm/s. $\frac{dP}{dL}$ is the pressure gradient, MPa/cm. $\frac{dP_0}{dL}$ is the threshold pressure gradient, namely, ISTP, MPa/cm. a and m are constants, m is generally > 1 when the fluid flow does not follow the Darcy law.

3.1.2. Fluid flow regimes

Apparent permeability, used to determine the onset of single-phase non-Darcy flow and to reflect the multiphase flow regimes, is sensitive to the fluid regime changes (Javadpour, 2009; Qiao et al., 2019; Singh et al., 2014; Zhang et al., 2016). Based on the downstream water flow rate, the water apparent permeability can be estimated using Eq. (2).

$$K_w = \frac{0.01 Q_w u_w L}{A \Delta P} \tag{2}$$

where K_w is the water apparent permeability, $\times 10^{-3}$ μm^2; Q_w is the water flow rate, ml/s; u_w is the water viscosity, mpa·s; L is the length of the cylindrical sample, cm; A is the cross-sectional area of the core plug, cm^2;ΔP is the differential pressure between the upstream and downstream, MPa.

The water permeability exhibits a quite similar trend to the variation of Q along with the increase of ΔP and time, in which two segments with different trends are identified successively, indicating different flow regimes (Fig. 4 A, C, E, G, I, K, M, O, Q). The inflection points on the water permeability curves, where apparent permeability values start to increase, capture the transition of UTFF regimes inside the cores, from which the ISTP can be precisely determined. The ISTP, corresponding to the greatest pressure before water permeability start to increase continuously, ranges widely from 0.28 to 4.56 MPa and is negatively correlated with permeability (Table 2). The ultimate water permeability, reflecting the maximum UTFF flow capacity, is in the wide range of 0.04–0.176 mD. To quantify the dynamic fluid flow capability (DFFC), the ratio of the maximum flow velocity increment and accumulative injection pressure increment, namely, ΔV/ΔP, is recorded, which is in the range of 0.00019–0.0073 cm/ (s·MPa). Generally, the DDFC rises with gas permeability, however, exceptions occur in some samples with high absolute permeability, which are probably attributed to the intricate pore structures.

For a better description of the non-Darcy or Pre-Darcy flow, the permeability-based Reynolds number (R_{ek}) is generally employed in the porous media with uncertain particle diameters (Chhabra, 2006; Comiti et al., 2000; Durlofsky and Brady, 1987; Farmani et al., 2018), which can be expressed in the following equation.

$$R_{ek} = \frac{\rho v \sqrt{k}}{\mu} \tag{3}$$

where ρ is the fluid density, g/cm^3; v is the fluid velocity, cm/s ; k is the gas permeability, 10^{-3} μm^2; μ is the fluid viscosity, mpa·s.

The Carman-Kozeny friction factor (f), primarily defined as a function of Reynolds number, is modified considering the permeability effect (Farmani et al., 2018), which can be described as following.

$$f = \frac{(\Delta P/L)\sqrt{k}}{\rho v^2} \tag{4}$$

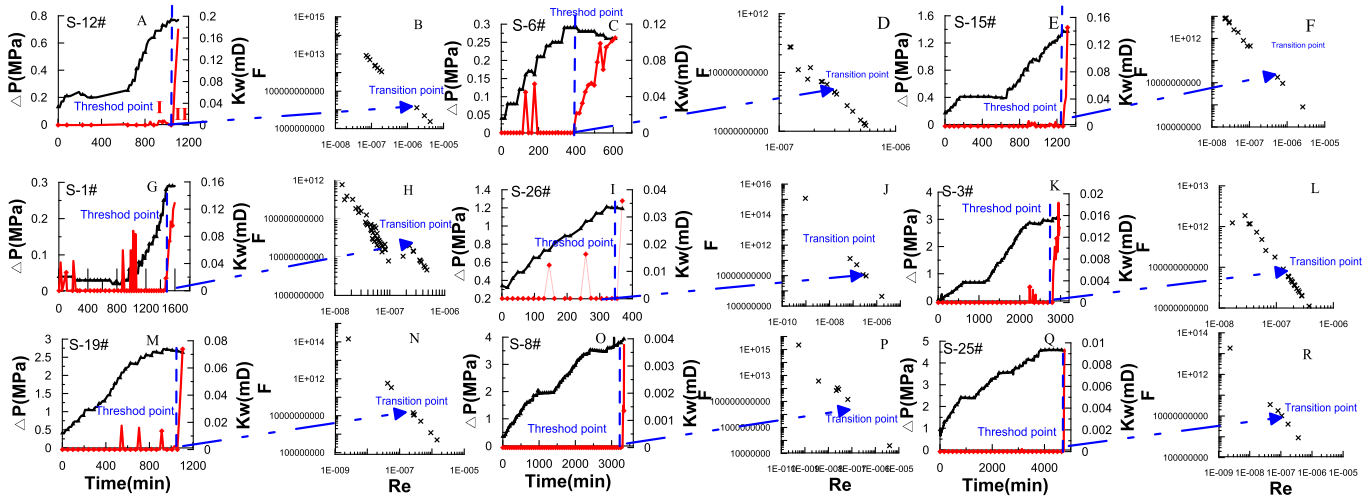

Fig. 4. Plots of time vs. differential injection pressure (△P) vs. water apparent permeability (A, C, E, G, I, K, M, O, Q) and plots of Reynolds number (R_{ek}) vs. fraction factor (f) (B, D, F, H, J, L, N, P, R) in the UTFF process.

Table 2
Characteristic parameters for the unsteady-state two-phase fluid flow.

Sample	ISTP, MPa	K_{wu}, mD	DFFC, cm/(s·MPa)
1#	0.29	0.129	0.0021
3#	3.05	0.018	0.00099
6#	0.28	0.105	0.00039
8#	3.93	0.004	0.00019
12#	0.73	0.176	0.0073
15#	1.37	0.145	0.0035
19#	2.66	0.047	0.00024
25#	4.56	0.009	0.0012
26#	1.19	0.036	0.0047

Note that ISTP refers to the threshold pressure for the start-up of the continuous non-wetting phase fluid intrusion; K_{wu} is the ultimate apparent water permeability of the unsteady-state fluid flow, DFFC is the dynamic fluid flow capability.

where $\Delta P/L$ is the differential pressure gradient, MPa/cm.

The R_{ek} vs. f plot is useful to identify the transitions between Pre-Darcy flow, Darcy, and Non-Darcy flow. Generally, the f shows a reversed linear correlation with R_{ek} in Darcy flow, the Pre-Darcy flow is characterized by a deviation from the linear correlation at low flow velocity, while the deviation at high flow velocity is known as Non-Darcy flow. Qiao et al. (2019) has reported that the relationships between Re and f of a single-phase fluid can effectively reflect the flow regimes and their transitions in the two-phase flow in the gas charging process.

The plots of R_{ek} vs. f for the water flow at downstream in the Fig. 4 exhibit deviations at the extreme low-velocity stage and obey negative linear correlations at a relative high flow rate, which are quite analogues to the Pre-Darcy flow. However, we should not confuse them. The transition points where the deviations disappear are almost in agreements with the inflection points on the water permeability curve, validating the credibility of the determination of the ISTP (Fig. 4 B, D, F, H, J, L, N, P, R).

3.2. Pore structure attributes

3.2.1. Experimental results

The evenly increasing trends of mercury saturation within the injection pressure range 100–10000 psi and corresponding even PSDs within the pore diameter of 0.01–10 μm of most of the samples (e.g. S-12#, S-15#, and S-26#) in Fig. 5 suggest even development of all sizes of pores in tight sandstone. The median intrusion pressures (P_{50}) and median pore diameters (D_{p50}) are in the range of 595.78–1929.44 psi (avg. 1167.77 psi) and 93.74–303.57 nm (avg.187.25 nm), respectively. Part of the samples (e.g. S-1#) show evident increments in the pressure interval of 0.1–100 psi, leading to the evident fraction increases of large-sized pores in the size range of 100–1000 μm, decreases in P_{50} (222.45 psi), and increases in D_{p50} (813.06 nm). Steeper segments are discovered in the pressure interval of 10000–100000 psi in some other samples (e.g. S-19#), resulting in volume fraction increases of tiny pores in the size range of 0.01–0.1 μm (Fig. 5 B). The P_{50}s increase sharply to the range of 5048.79–8217.74 psi (avg. 6633.26 psi) and D_{p50}s decrease to

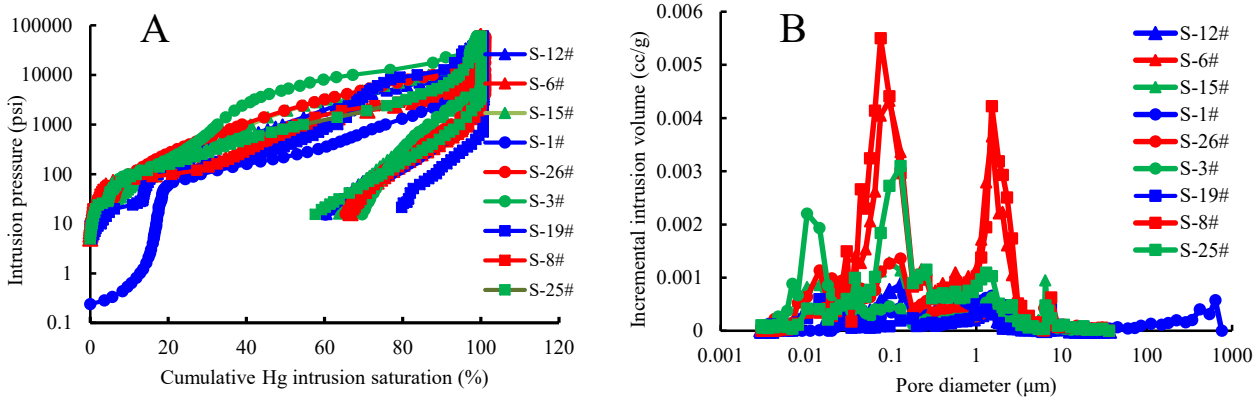

Fig. 5. Mercury intrusion and extrusion curves of PCP and converted pore diameter distributions.

22.01–35.82 nm (avg. 28.92 nm).

The wide T_{2s} distributions agree well with the PSDs measured by PCP and are characterized by different distribution patterns (Fig. 6 A, C, E, G, I, K, M, O, Q). With decreasing permeability, the patterns of T_{2s} changes from bimodal to unimodal, accompanied by the shift of major peaks from 10 to 2 ms. Simultaneously, the amplitudes of the secondary right peaks reduce, indicating reductions of the large-sized pores. Amplitude differences between the T_{2s} and T_{2c} are defined as movable signals. Unimodal distributions are found in the movable signals in the samples with permeability > 0.1 mD, but they become complicated when the permeability < 0.1 mD. To quantify the connective degree of certain-sized pores, the ratio of movable signal to the saturation signal at certain T_2 value is defined as movable proportion (Fig. 6 B, D, F, H, J, L, N, P, R). The movable proportion is positively correlated with T_2 (i.e. pore size) when the permeability > 0.1 mD (Fig. 6 B, D, F, H, J, L), but has an extreme complex correlation with it when the permeability < 0.1 mD (Fig. 6 N, P, R). The pores with T_2 > 100 ms exhibit best connectivity with movable proportions > 0.6, most of which are close to 1 in the samples with permeability > 0.1 mD. The connectivity reduces with decreasing pore size, of which the pores in the T_2 range of 1–100 ms are partly connected, with movable proportion between 0.4 and 1.0, while those with T_2 < 1 ms can hardly be connected, with most of the proportions < 0.1 and close to 0. The connectivity of same-sized pores shows a rising trend with increasing permeability. Notably, the presences of negative movable proportion values are attributed to the water redistribution from large-sized to small-sized pores under the centrifugal force.

The segmented binary images displaying the pore spatial distribution, modelled ball-stick skeleton graphs showing the pore-throat connection and combination, and merged pore-throat radii distributions derived from X-μCT are displayed in Fig. 7. Image descriptions suggest that the connected large-sized pores construct the major structure of the pore system, while the tiny pores are mostly isolated in space, part of them may be connected to the major network but only serve as dead ends (Fig. 7). With decreasing permeability, the bulk volumes and connectivity of the major structures reduce owing to the pore size reduction and connection losses. The pore-throat radii distribution histograms give out quantitative description of the pore connectivity, in which the yellow parts represent the connective proportions of the pores of certain size (pores with calculated coordination number > 0), while the blue parts (pores with calculated coordination number = 0) are on the opposite. The connectivity rises with pore size, of which the pores with radii < 20 μm are mostly disconnected, those of 20–100 μm are partly connected, while those with size > 100 μm are almost fully connected. The same-sized pores show connectivity reductions with decrease of permeability, particularly in the pores with radii > 20 μm. However, the reliability and applicability of the X-μCT information are restricted to some extent owing to the resolution effects and representative voxel selection.

3.2.2. *Full-range pore size distribution*

The PSDs of tight sandstone measured by PCP, NMR, and X-μCT are reliable in different size range. An accurate acquisition of the full-range pore size distribution (FPSD) depends on the proper integration of multiple methods (Lai et al., 2018b; Loucks et al., 2009; Nelson, 2009; Xiao et al., 2017). Prior to the merge, the T_2 signal has to be converted to pore size, which relies on the ρ determination that can be calibrated by the relations between the accumulative pore size distribution of PCP and accumulative incremental porosity curve of T_{2s} (Fig. 8 A, B). The processing method used in the determination of ρ by calibrating the results of PCP and NMR has been thoroughly explained in recent publications, which would not be introduced in our paper for simplicity (Kleinberg, 1996; Mohnke, 2014; Torrey, 1956).

The PSDs measured by the three methods are plotted together in the same coordinate in Fig. 8. We can discover that the NMR PSDs agree well with the PCP PSDs but show a few differences in the range of 1–100 μm, however, those of X-μCT are distinct, which are attributed to the scanning resolution of 3 μm (Fig. 8 B, E, H). In the merging process, the FPSDs should follow the NMR PSDs in the size range where the PSDs of NMR and PCP almost coincide, generally in the range of 0.001–1 μm, because NMR is more credible as it is non-destructive. The incremental proportions of pores need to be averaged in the range where the PSDs of NMR and PCP differentiate, commonly in the range of 1–10 μm, to reduce the potential systematic differences. Coming to the range of 1–1000 μm, all of the three PSDs present, averaging should be conducted on the three PSDs by taking the sampling influences into account (Fig. 8 B, E, H). The merged FPSDs are multimodal in the extreme wide range between 10 nm and 1000 μm, showing three peaks at around 0.1, 1, and 200–500 μm, suggesting a highly complex pore constitute with presences of pores from nanometer to millimeter (Fig. 8 C, F, I). The FPSDs

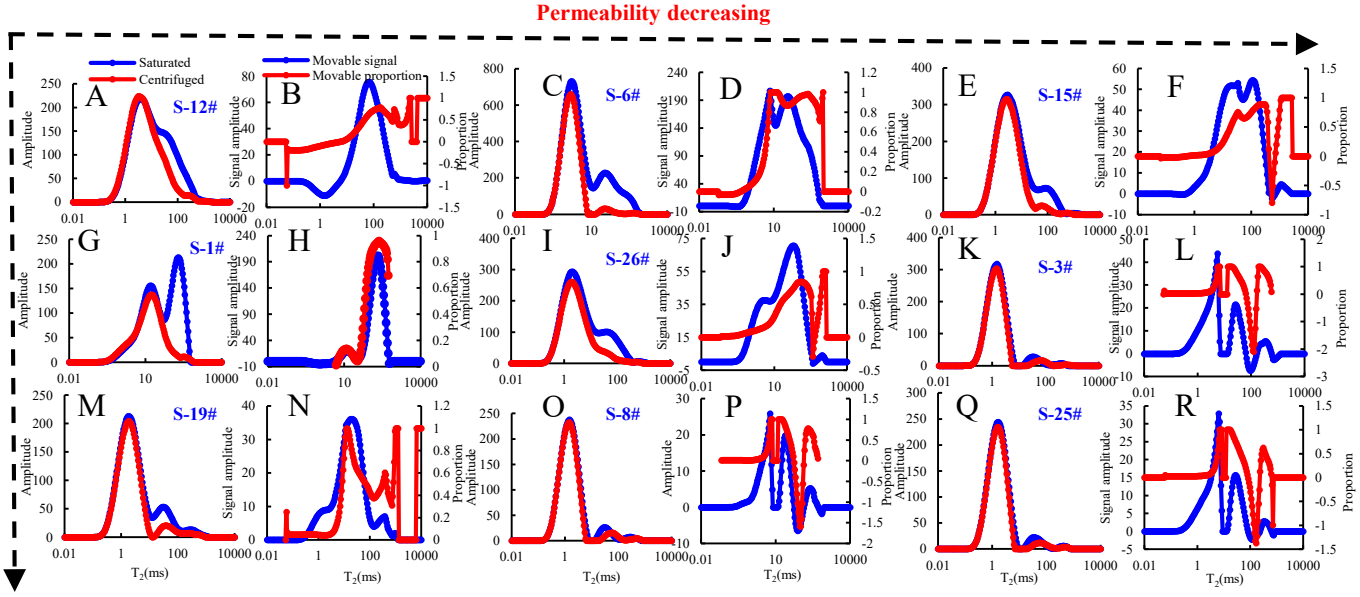

Fig. 6. NMR T_2 spectrums of the tight porous sandstone under the saturated and centrifuged states (A, C, E, G, I, K, M, O, Q). Movable signal amplitude and movable proportion identified from the T_2 distributions before and after centrifugation (B, D, F, H, J, L, N, P, R).

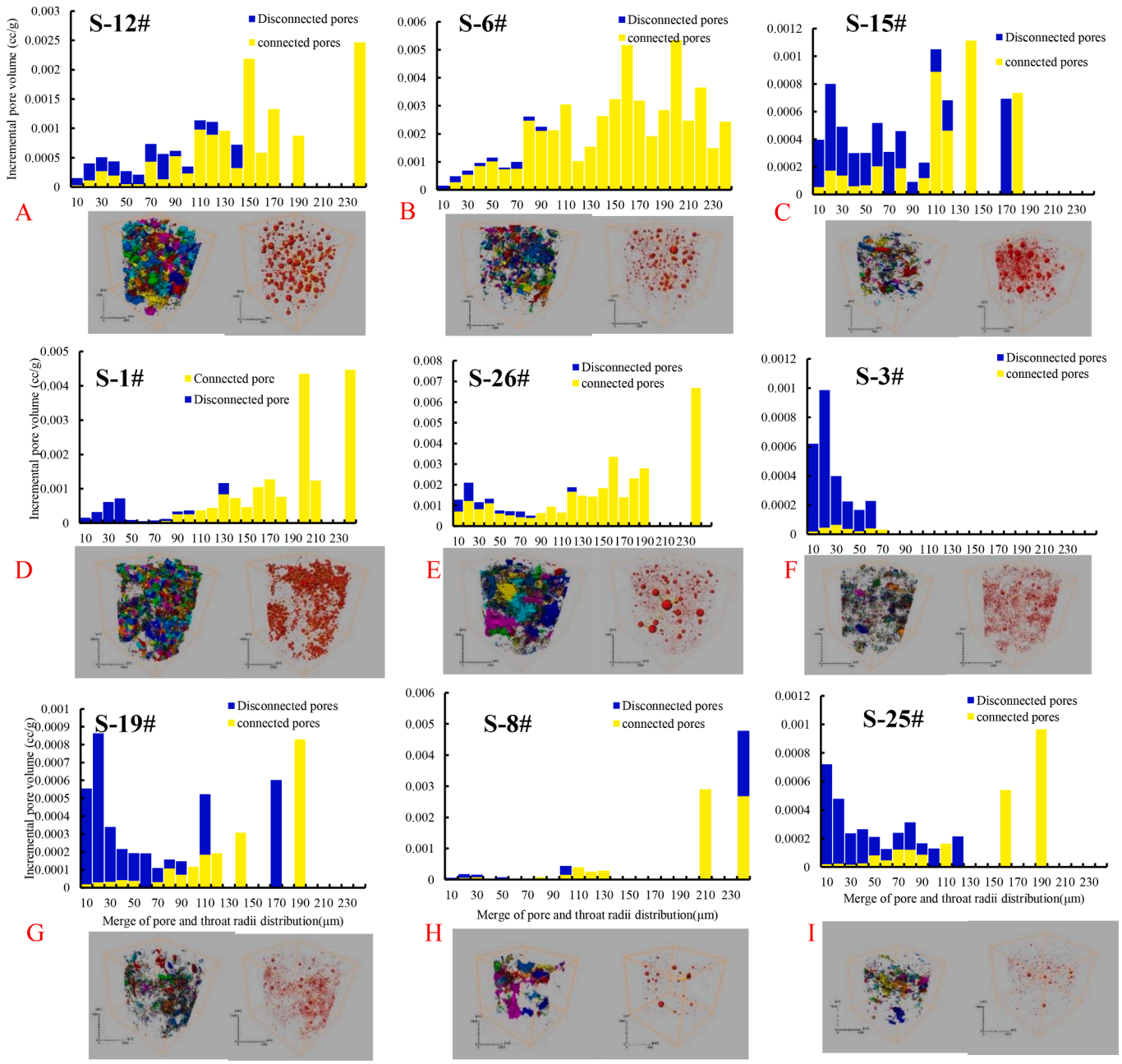

Fig. 7. The three-dimensional pore spatial distribution (color-labeled images), skeleton pore-throat network (ball-stick images, where the red sphere represents pore and yellow stick presents throat), and merged pore-throat radii distribution histograms (the yellow part corresponds to the connected proportion of pores in certain size and blue part corresponds to their disconnected proportion) obtained from X-μCT. (For interpretation of the references to color in this figure legend, the reader is referred to the web version of this article.)

vary with decreasing permeability, of which the three major peaks become left-skewed and amplitudes of the two right peaks reduces evidently, indicating the narrowing of the pore and throat spaces. All sizes of pores have contributions to the storage spaces for the samples with permeability > 0.1mD, but the nanopores (10 nm-1 μm) and micro-small pores (1–10 μm) dominate the porosities of the samples with permeability < 0.1 mD.

3.2.3. *Pore connectivity*

As connected pore space dominates the fluid flow, pore connectivity is more crucial in low-connectivity tight porous media with complex pore structure, but discussions on it are limited due to the difficulties in measurement and quantification. As indicated, NMR and X-μCT provide quantitative pore connectivity description information as the connective ratios of pores of certain sizes can be determined by the movable proportions of NMR and obtained by calculating the volume fraction of pores with coordination number > 0 in X-μCT, respectively. The connective ratio distributions of the two techniques are plotted together in a same coordinate, from which piecewise function relations are discovered between the pore size and the ratio (Fig. 9, Table 3). The connectivity of the pores in the size range 0.001–0.1 μm generally has positive polynomial correlations with their sizes. The plots are fluctuated in the range 0.1–10 μm, where two or three polynomial correlations can coexist. The segment points of these piecewise functions in this range are generally at 1.0 μm and will be left-skewed with permeability reduction. The connectivity of the pores > 10.0 μm commonly has positive correlations with diameters and connective ratio is generally equal to 1 when diameter > 20.0 μm. However, reverse correlations are discovered in the

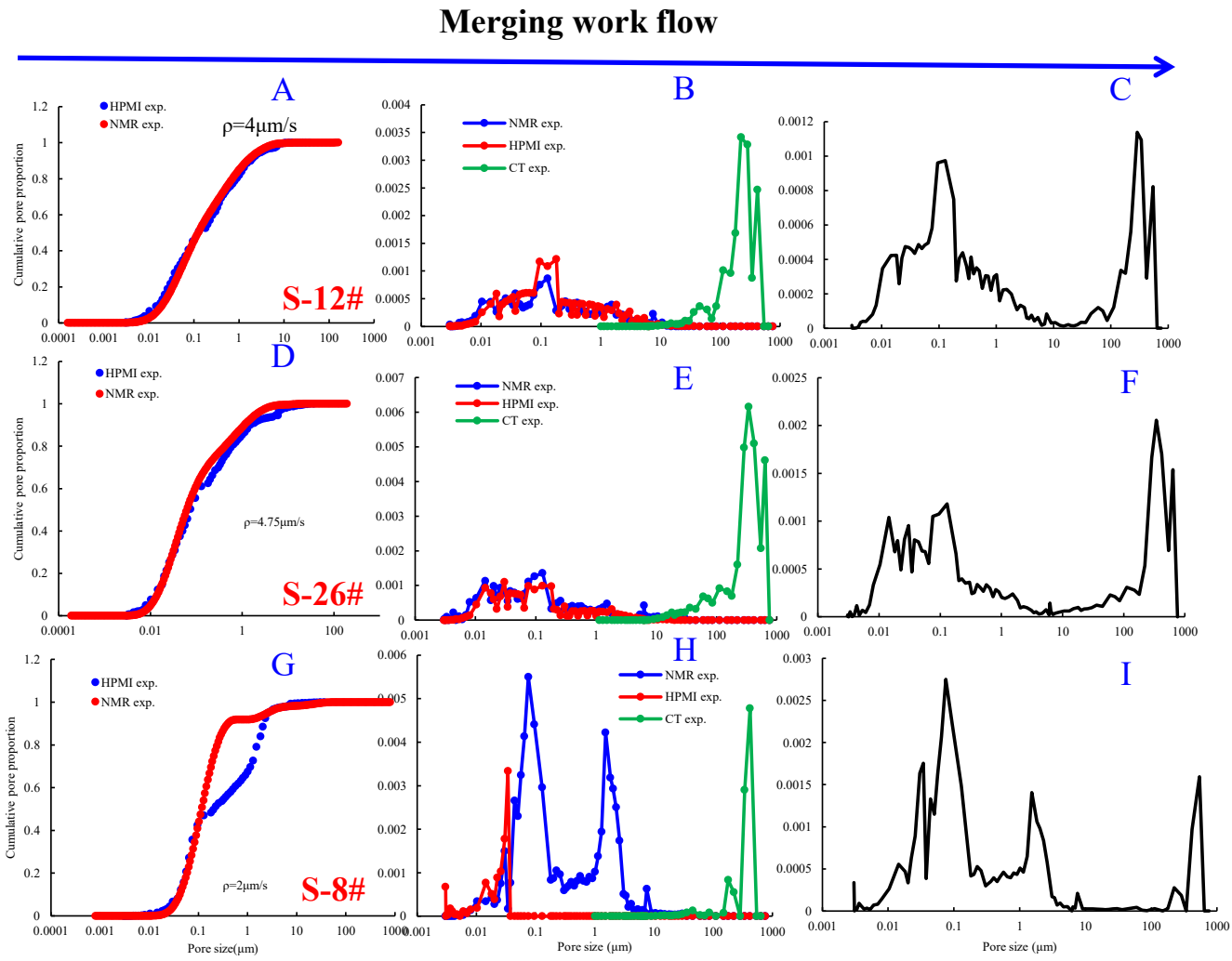

Fig. 8. Determination of surface relaxation ratio employing the cumulative mercury intrusion curve of PCP and cumulative incremetal porosity curve obtained from T_{2s} spetrum (A, D, and G). Three types of PSD separately derived from the NMR, PCP, and X-μCT plotted in the same coordinate (B, E, and H). FPSD obtained by merging the three types of PSDs (C, F, and I).

samples with ultra-low permeability, e.g. S-8# and S-25#, which may probably attributed the blockage of connected pathways between the large pore voids. The connectivity of pores with sizes > 100 μm is given out by X-μCT and generally shows positive polynomial relationships with their diameters and is commonly close to 1 with increasing pore size (Fig. 9 A-I). Notably, the connectivity evaluations of NMR and X-μCT coincide in the pore size rang 10–100 μm, however, the indirect X-μCT results are not taken into account as they are strongly affected by the resolution and scanning voxel, while the direct NMR measurements are believed to be more credible in this range in comparison.

The pore connectivity evaluation enables us to figure out the connected FPSDs (CFPSDs) by multiplying the volume fractions of certain-sized pores on FPSDs and connective ratios obtained from the correlations in the piecewise functions in the Fig. 9 (Table 3). The CFPSDs of most of the tight sandstone samples are characterized by right-skewed unimodal distribution patterns, in which the high amplitudes on the right of the X-axis and low amplitudes in the range 0.1–100 μm suggest the system connectivity is dominated by the pores with sizes > 100 μm (Fig. 10). Bimodal CFPSD distribution patterns occur in the samples S-6#, S-8#, and S-25# with two peaks in the range of 0.1–10 μm and 100–1000 μm, respectively. The connectivity increases in these small-sized pores may be attributed to the extra connections provided by the micro fractures to small void spaces. As the fluid flow pathway is constructed by the connected pore spaces in terms of fluid flow, therefore, the key structural parameters are recorded on the basis of the CFPSDs. The D_{cmin}, D_{c50}, and λ_{max} separately referring to the minimum, median, and maximum connected pore diameters are listed in Table 4. The D_{cmin} is between 3 and 129 nm (avg. 30.26 nm), D_{c50} ranges from 302.5 nm to 283.3 μm (avg. 70.19 μm), and λ_{max} is in the range 120.3–629.61 μm (avg. 438.59 μm). The variations of mean parameter indicate evident differences in the connected flow pathways in tight porous sandstone and the positive correlations between these parameters and permeability suggest that the better connectivity is always favorable for the fluid flow capacity. The connected proportion ranges from 0.15 to 0.55 (avg. 0.33), suggesting low connective degrees and huge connectivity variations of tight porous sandstone.

3.2.4. *Microscopic heterogeneity of the connected pore system*

Pore fractal dimension has been admitted as an effective parameter to describe the complexity and heterogeneity of microstructures. The determination of pore fractal dimension using the PSDs obtained from different techniques has been thoroughly explored and explained according to the fractal principle, of which the number of pores with radii > r (N(r)) has a positive correlation with pore radius r, i.e. $N(r) \propto r^{-Df}$ (Bale and Schmidt, 1984; Lai et al., 2018a; Mandelbrot, 1975; Mandelbrot et al., 1984; Qiao et al., 2021). Generally, the D_f for pores in certain

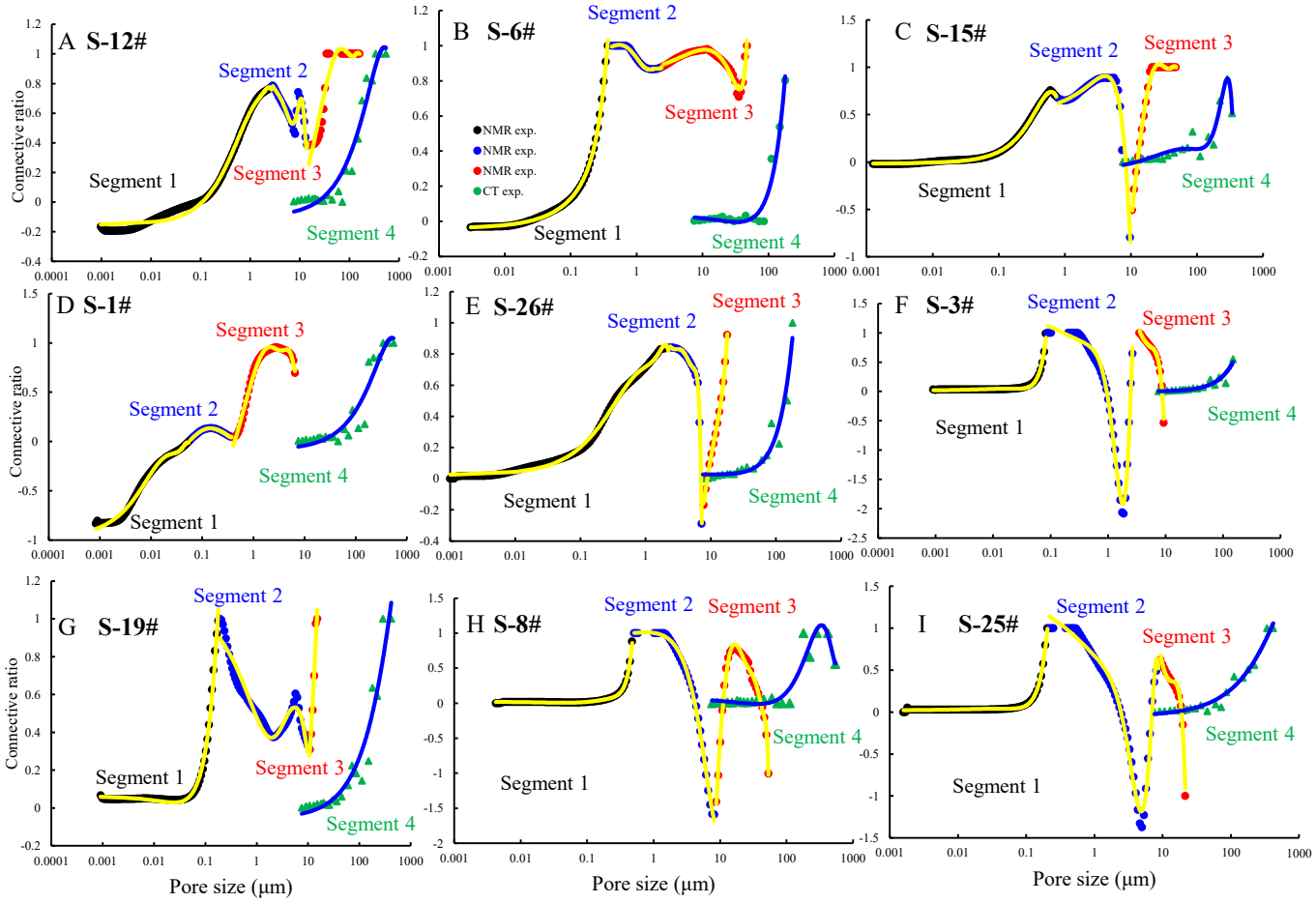

Fig. 9. Pore connectivity evaluation according to the correlations between pore size and its connective ratio acquired from the NMR and X-μCT analyses, respectively.

size range equals to the 3-K, where K is the slope of the linear segments on the lg (S_r) vs lg (D) plots, according to the correlation of $S_r = (\frac{D}{D_{max}})^{3-Df}$ that is derived from the fractal principle and relations between N(r) and pore volume fraction (note that the S_r is the cumulative volume fraction for the pores with radii < r (diameter < D)) (Fig. 11). The detailed derivation procedures can refer to the studies of Li and Horne (2006), Lai et al. (2018a,b), and Qiao et al. (2021), which will not be explained in this work for simplicity. The segmented linear plots in Fig. 11 suggest that the tight porous sandstone is characterized by highly heterogeneous microstructure with common tri-fractal structure. D_{1c}, D_{2c}, and D_{3c}, rising successively with increasing pore size, can be obtained (Table 4). The D_{1c} for the small-sized pores varies widely between 0.13 and 2.04, suggesting that theses pores are not fractal but are intensely heterogeneous, D_{2c} for medium-sized pores is in a narrow range of 1.48–2.38 and has a greater dimension value close to 2, indicating increases in self-similarity and homogeneity, while D_{3c} for the large-sized pores exhibits very little fluctuations in the range of 2.82–2.97, suggesting a high homogeneity of these pores. The D_{avg}, mean of the D_{1c}, D_{2c}, and D_{3c}, ranges widely from 1.66 to 2.29, indicating significant differences in the microscopic heterogeneities of the connected fluid flow pathways.

3.3. Insights into the UTFF in the nano-micrometer pore system

3.3.1. Relationships between the pore structure and UTFF

The dynamic fluid flow strongly depends on the microstructural attributes of connected pore network, especially for the tight porous media with nano-micrometer pore size and intense heterogeneity. To investigate the effects of the pore structures on the dynamic UTFF inside it, the correlations between the key structural parameters for the connected pore networks and critical parameters for the UTFF, including the ISTPs, average fluid velocity obtained by averaging the water flow velocity from the beginning to ending, average DFFC describing the ratio of total velocity increment to the total injection pressure increment from the beginning ($\Delta V/\Delta P$), and ultimate water permeability that is the apparent water permeability at the end of UTFF experiment, are explored (Figs. 12, 13). These correlations and their correlative coefficients show that increasing pore sizes, e.g. D_{cmin}, D_{c50}, and λ_{cmax}, would reduce the ISTPs and increase the average fluid velocity, average DFFC, and ultimate water permeability (Figs. 12 A-C, 13 A-C), while the D_{avg} and tortuosity τ_c exert opposite effects, of which τ_c shows greater impacts than D_{avg} (Figs. 12 D, E, 13 D-H). According to the correlations in Figs. 12 and 13, it can be deduced that the narrowing and heterogeneity and actual flow length increases of the connected pathways will increase the flow resistance and result in evident fluid velocity loss of UTFF in the primary gas charging or intrusion. The higher correlation coefficients of the negative correlation between D_{c50} and ISTP, and those of the positive correlations between D_{c50}, average fluid velocity, DFFC, and ultimate water apparent permeability suggest the average sizes of the flow pathways control the UTFF in tight porous media (Figs. 12 B, 13 A-C). Notably, instead of pore size, the heterogeneities exert extra controls on the ISTPs of UTFF in the case of the $D_{c50} < 10$ μm, which can be supported by the stronger positive correlations between D_1, D_{avg}, and ISTPs (Fig. 12 A, B, E). The UTFF in the extreme tight porous sandstone is controlled by the pore geometry and topology in couple, supporting by the poorer correlations between D_{avg} and ISTP, and better relations

Table 3
Equations describing the correlations between pore connectivity and pore size.

Sample	Fitting function 1	Fitting function 2	Fitting function 3	Fitting function 4
1#	$y = -671775x^4 + 93971x^3 - 4689.8x^2 + 102.68x - 0.968$ ($R^2 = 0.9921$)	$y = 545.07x^5 - 699.3x^4 + 359.39x^3 - 92.575x^2 + 11.469x - 0.4041$ ($R^2 = 0.9996$)	$y = 0.0025x^5 - 0.053x^4 + 0.425x^3 - 1.6088x^2 + 2.8617x - 0.9627$ ($R^2 = 0.9903$)	$y = -4E\text{-}06x^2 + 0.0044x - 0.0854$ ($R^2 = 0.9138$)
3#	$y = 3686.3x^3 - 233.64x^2 + 4.7726x + 0.0162$ ($R^2 = 0.9901$)	$y = -0.7781x^5 + 5.1881x^4 - 10.987x^3 + 8.2603x^2 - 3.1699x + 1.3431$ ($R^2 = 0.9901$)	$y = -0.0193x^3 + 0.3233x^2 - 1.8594x + 4.4189$ ($R^2 = 0.9899$)	$y = 0.0002x^{1.5783}$ ($R^2 = 0.9081$)
6#	$y = 13.596x^3 - 1.6743x^2 + 1.7201x - 0.0388$ ($R^2 = 0.999$)	$y = 0.0697x^6 - 0.4751x^5 + 1.0571x^4 - 0.5326x^3 - 0.9586x^2 + 1.0245x + 0.7456$ ($R^2 = 0.996$)	$y = 2E\text{-}08x^5 - 2E\text{-}06x^4 + 9E\text{-}05x^3 - 0.0028x^2 + 0.0361x + 0.8179$ ($R^2 = 0.9415$)	$y = 4E\text{-}05x^2 - 0.0026x + 0.0393$ ($R^2 = 0.964$)
8#	$y = 67.674x^4 - 43.19x^3 + 10.437x^2 - 0.7028x + 0.0207$ ($R^2 = 0.9978$)	$y = 0.0096x^3 - 0.1423x^2 + 0.1997x + 0.9372$ ($R^2 = 0.9979$)	$y = -3E\text{-}08x^6 + 6E\text{-}06x^5 - 0.0005x^4 + 0.0205x^3 - 0.4668x^2 + 5.4579x - 24.617$ ($R^2 = 0.9932$)	$y = 2E\text{-}10x^4 - 2E\text{-}07x^3 + 7E\text{-}05x^2 - 0.0046x + 0.0695$ ($R^2 = 0.9039$)
12#	$y = -0.058x^4 + 0.4136x^3 - 1.1438x^2 + 1.5509x - 0.1534$ ($R^2 = 0.991$)	$y = 3E\text{-}05x^6 - 0.0012x^5 + 0.021x^4 - 0.1814x^3 + 0.8182x^2 - 1.9124x + 2.6122$ ($R^2 = 0.8948$)	$y = -1E\text{-}08x^4 + 6E\text{-}06x^3 - 0.001x^2 + 0.0653x - 0.5316$ ($R^2 = 0.9118$)	$y = -5E\text{-}06x^2 + 0.0045x - 0.0978$ ($R^2 = 0.9548$)
15#	$y = 3.0442x^4 - 7.7903x^3 + 4.1869x^2 + 0.8924x - 0.0156$ ($R^2 = 0.999$)	$y = -0.0031x^3 + 0.0014x^2 + 0.1442x + 0.508$ ($R^2 = 0.9647$)	$y = -5E\text{-}06x^4 + 0.0007x^3 - 0.0353x^2 + 0.8188x - 5.9103$ ($R^2 = 0.9953$)	$y = -1E\text{-}09x^4 + 8E\text{-}07x^3 - 0.0001x^2 + 0.0097x - 0.0975$ ($R^2 = 0.9303$)
19#	$y = -61.707x^3 + 57.053x^2 - 2.6741x + 0.0613$ ($R^2 = 0.9946$)	$y = 3E\text{-}05x^6 - 0.0011x^5 + 0.0165x^4 - 0.128x^3 + 0.5265x^2 - 1.0059x + 1.0713$ ($R^2 = 0.9353$)	$y = -0.0017x^2 + 0.2164x - 1.8532$ ($R^2 = 0.9636$)	$y = -2E\text{-}06x^2 + 0.0034x - 0.0554$ ($R^2 = 0.9315$)
25#	$y = 232.21x^3 - 31.032x^2 + 1.362x + 0.0206$ ($R^2 = 0.9962$)	$y = 0.0003x^6 - 0.0086x^5 + 0.0997x^4 - 0.4921x^3 + 1.054x^2 - 1.3755x + 1.3923$ ($R^2 = 0.9869$)	$y = -0.0029x^3 + 0.1231x^2 - 1.723x + 8.4272$ ($R^2 = 0.9752$)	$y = -2E\text{-}06x^2 + 0.0033x - 0.0475$ ($R^2 = 0.9694$)
26#	$y = -0.224x^4 + 1.1884x^3 - 2.2751x^2 + 2.0058x + 0.023$ ($R^2 = 0.9972$)	$y = -0.0062x^5 + 0.1317x^4 - 1.0883x^3 + 4.3568x^2 - 8.4656x + 7.2394$ ($R^2 = 0.9991$)	$y = 0.0012x^3 - 0.0442x^2 + 0.6408x - 3.0166$ ($R^2 = 0.9996$)	$y = 3E\text{-}05x^2 - 0.0005x + 0.0297$ ($R^2 = 0.9384$)

Note that the equations 1, 2, 3, and 4 separately correspond to the fitting functions for the segments 1, 2, 3, and 4 in the plots of connective ratio vs. pore size in Fig. 9.

between τ and ISTP (Fig. 12 D, E).

3.3.2. Gas accessibility in the nano-micrometer pore systems

The gas flow behaviors in the UTFF could not be determined directly owing to the specialties of the primary gas intrusion or charging process and experiment design. In order to investigate the gas accessibilities in the nano-micrometer pore systems, the water layer theory and effective percolation radius are combined and applied. The water layer distribution model stems from the DLVO (Derjaguin-Landau-Verwey-Overbeek) theory that describes the interactions between the solid surface and aqueous solution employing the disjoining pressure (Churaev, 2003; Lebeau and Konrad, 2010; Woodruff and Revil, 2011; Yang and Yu, 2020). The disjoining pressure is composed of a short-range van der Waals force, long-range electrostatic force, and structural force under the equilibrium condition, which can be expressed as following (Israelachvili, 2015; Lebeau and Konrad, 2010; Tuller and Or, 2003).

$$\Pi(h) = \Pi_m(h) + \Pi_e(h) + \Pi_s(h) \tag{6}$$

$$\Pi_m(h) = \frac{A_{12}}{6\pi h^3} \tag{7}$$

$$\Pi_e(h) = \frac{\varepsilon_0 \varepsilon_r}{2}\left(\frac{\pi k_B T}{ez}\right)\frac{1}{h^2} \tag{8}$$

$$\Pi_s(h) = Ke^{-\frac{h}{\lambda}} \tag{9}$$

$$A_{12} \approx \sqrt{A_{11}A_{22}} \tag{10}$$

where $\Pi(h)$is the disjoining pressure, $\Pi_m(h)$ is the Van der Walls force, $\Pi_e(h)$ is the electrostatic force, $\Pi_s(h)$ is the structural force, h is the distance from the solid surface, and A_{12} is the Hamaker constant for the intersections between solid substrate (A_{11}) and water (A_{22}). The physical constants used for calculating the interfacial of water/tight sandstone interactions are listed in Table 5. Note that the A_{11} can be estimated according to the mineral constitutes acquired from XRD results in Table 1 and Hamaker constants for them.

The contributions of the three kinds of forces to the disjoining pressure are illustrated in Fig. 14 (e.g. S-1#, S-3#, S-6#). Considering the interfacial forces acting on the water molecules, the water in water-saturated pores can be divided into four parts in the direction perpendicular to the solid surfaces, including the free water layer (FW), outer layer of weakly bound water (OBW), inner layer of weakly bound water (IBW), and strongly bound water layer (SBW) (Yang and Yu, 2020) (Fig. 14 A). It has been reported that the FW is not subjected to the surface force, only existing in the pore zones that exceed the free plane (fp). The distance from the surface to the fp can has been indicated by Debye length in shale, approximate 960 nm (Yang and Yu, 2020), and is approximate 1509.96 nm estimated by disjoining pressure in our investigation. This calculation suggests that the FW can only exist in the centers of the pores with diameters > 3020 nm (2fp) in tight porous sandstone. Water in the OBW, occurring in the pore zones ranging threshold plane (tp) to fp, mainly held by the electrostatic force, is less affected by the solid surface, and can flow under small pressure gradients. The length of solid surface to tp can be obtained by determining the cross point of the electrostatic force and structural force, whereby the thickness of the OBW can be determined by combining the lengths of fp and tp (Table 6). The water in the IBW, confining between the shear plane (sp) and tp, is controlled by molecular, electrostatic, and structural forces, which is commonly considered to be immovable when the displacement pressure < TPG but is potentially movable when the pressure > TPG. The length of solid surface to sp can be calculated by the cross point of the Van der Walls force and electrostatic force, whereby the thickness of IBW can be determined. Water in the SBW is strongly absorbed to the solid surface and is particularly immovable, whose thickness is confined by the sp ranging from 0.77 to 0.97 nm (Table 6).

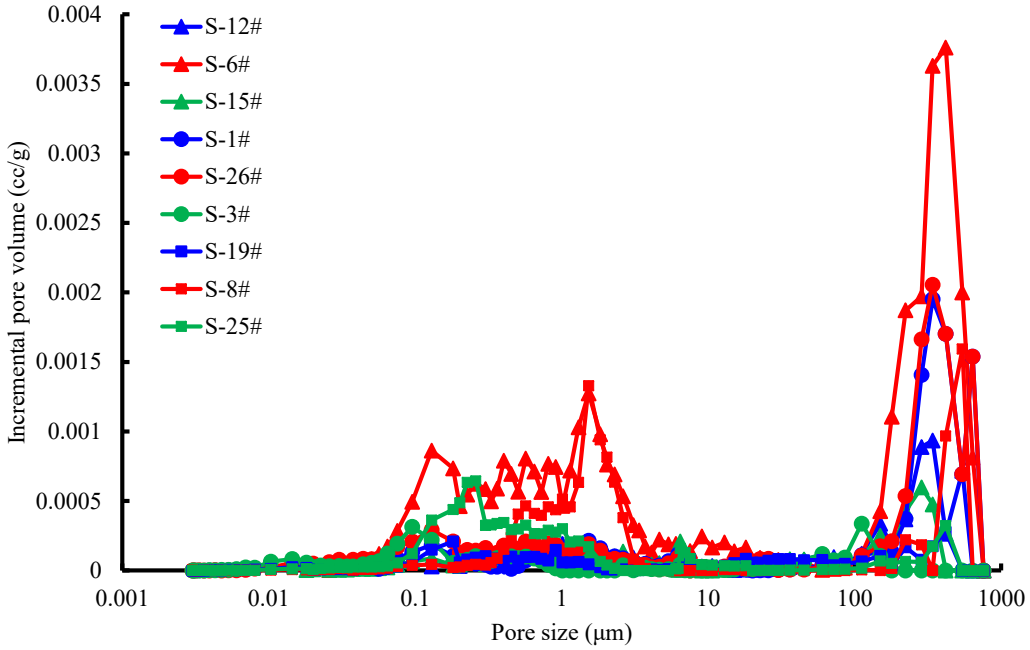

Fig. 10. CFPSD of the tight porous sandstone.

Table 4
Pore structure parameters.

Sample	ρ, μm/ms	D_{50}, μm	D_{c50}, μm	D_{cmin}, μm	λ_{cmax}, μm	D_{1c}	D_{2c}	D_{3c}	D_{avgc}	τ_c	C
1#	6.0	1.53	222.45	0.057	512.62	0.45	2.33	2.79	1.95	3.89	0.55
3#	7.5	0.095	0.30	0.0030	120.30	0.22	2.21	2.92	1.78	4.70	0.15
6#	25.0	0.36	4.12	0.026	596.60	0.13	2.04	2.87	1.68	2.66	0.55
8#	4.0	0.075	1.52	0.0030	504.17	2.04	1.49	2.97	2.17	4.72	0.26
12#	8.0	0.30	111.79	0.13	511.65	0.68	2.48	2.83	1.99	3.68	0.32
15#	9.0	0.023	6.46	0.018	340.26	1.64	2.15	2.85	2.21	3.90	0.22
19#	7.5	0.095	1.30	0.0030	361.76	1.34	2.17	2.88	2.13	4.26	0.39
25#	15.0	0.13	0.40	0.0030	370.39	1.52	2.39	2.97	2.29	6.12	0.28
26#	9.5	0.30	283.34	0.0030	629.61	0.32	1.84	2.82	1.66	3.14	0.47

Note that ρ refers to the surface relaxation ratio, D_{50} is the median pore diameter derived from the FPSD. D_{c50}, D_{cmin}, and λ_{cmax} separately correspond to the median, minimum, and maximum pore diameters obtained from the CFPSD. D_{1c}, D_{2c}, and D_{3c} are the fractal dimensions for the small-sized, medium-sized, and large-sized pores obtained from the CFPSD. Davg is the mean of D_{1c}, D_{2c}, and D_{3c}. τ_c is the tortuosity derived from the CFPSD and C is the connective proportion.

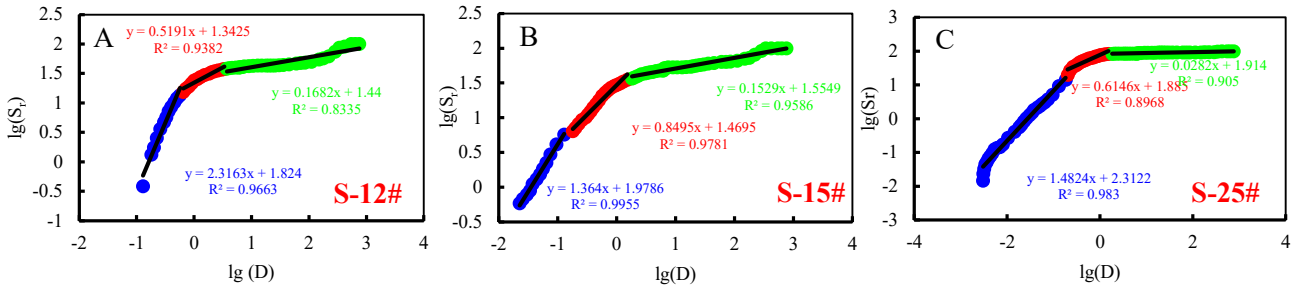

Fig. 11. Overall fractal characteristics of connected pore system in tight porous sandstone built on the basis of the CFPSD.

The four types of water layers can only coexist in the pores with diameter > 2fp, where the water flow can occur under a pressure gradient no matter how small it is. For the pores with diameters in the range of 2tp-2fp, there are extra pressure needs for the water movement. However, for the pores with sizes between 2sp and 2tp, the fluid can flow only when the pressure gradient > TPG, while the pores with diameters < 2sp do not contribute to the fluid flow. It can be deduced that the presences of the pores with diameter ranging from 2sp to 2tp in the connected fluid flow pathways result in the existences of TPG in single-phase flow and ISTP for UTFF, and successive water movement in the FW, OBW, and IBW zones are responsible for the increases of the effective radius and apparent permeability in the multiphase fluid flow. Particularly, the fluid flows in OBW and IBW zones dominate the effective radius and apparent permeability increases of the continuous single- or multi-phase flow in tight porous media.

Combining the CFPSDs and water layer thicknesses on the basis of the circular pore assumption, the distributions of water layers under saturated condition in different-sized connected pores can be obtained, whereby the ratios for different water layers in certain-sized pores can be derived using the Eqs. (11)–(14) to describe the potential static fluid

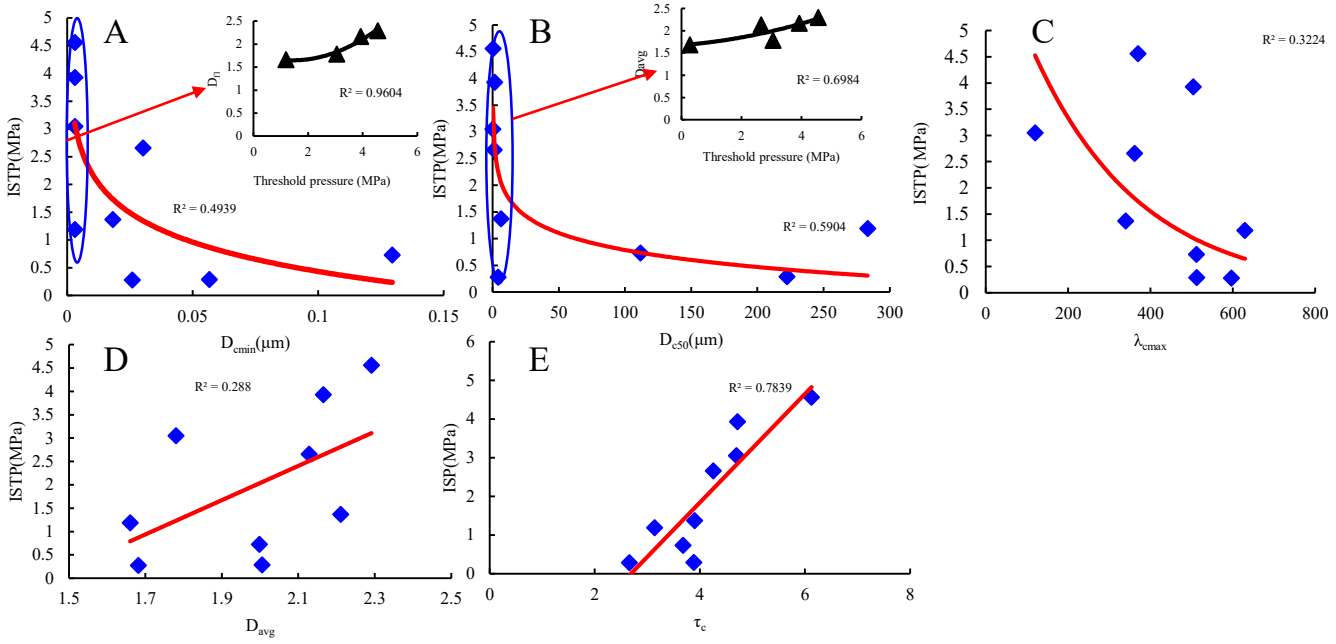

Fig. 12. Correlations between the pore structure characteristics and ISTP in the UTFF procedure.

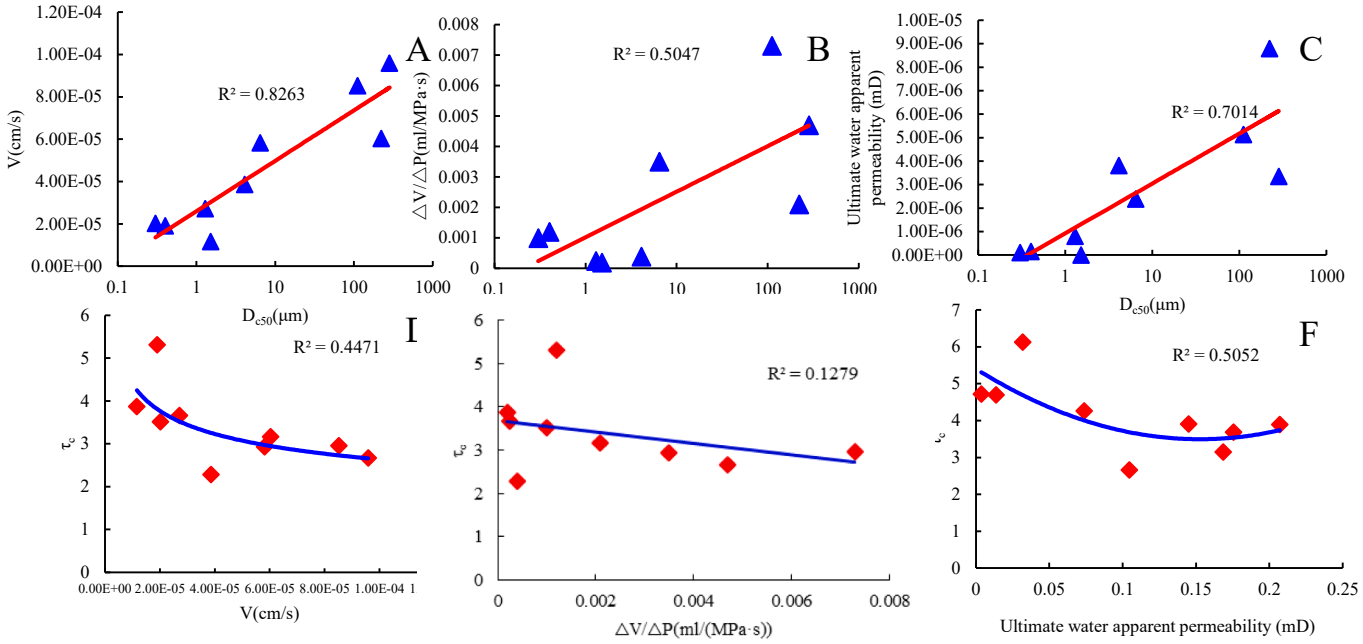

Fig. 13. Effects of D_{c50} and τ_c of the connected pore system on the dynamic fluid flow behaviors of the UTFF.

mobility in tight porous sandstone (Fig. 15). As shown in Fig. 15, there are only SBW and IBW exist in the pores with diameters < 40 nm (generally radii < the sum of r_{SBW} and r_{IBW}), SBW, IBW, and OBW present in the pores with diameters between 40 and 3020 nm, while the four types of layers coexist in the pores with diameters > 3020 nm. The presences of the pores < 40 nm in the connected flow pathway result in the existences of the ISTPs in UTFF.

$$R_{SBW} = 1 - (1 - \frac{sp}{r})^2 \tag{11}$$

$$R_{IBW} = \begin{cases} \left(1 - \frac{sp}{r}\right)^2 & if\ \ sp < r < tp \\ \left(1 - \frac{sp}{r}\right)^2 - \left(1 - \frac{tp}{r}\right)^2 & if\ \ r > tp \end{cases} \tag{12}$$

$$R_{OBW} = \begin{cases} 0 & if\ \ r < tp \\ \left(1 - \frac{tp}{r}\right)^2 & if\ \ tp < r < fp \\ \left(1 - \frac{tp}{r}\right)^2 - \left(1 - \frac{fp}{r}\right)^2 & if\ \ r > fp \end{cases} \tag{13}$$

Table 5
Physical constants for the calculation of disjoining pressure (Yang and Yu, 2020).

Constant	Symbol	Value	Unit
Hamaker constant(quartz)	A_{11Q}	6.8×10^{-20}	J
Hamaker constant(calcite)	A_{11Ca}	1.2×10^{-19}	J
Hamaker constant(illite)	A_{11I}	1.8×10^{-19}	J
Hamaker constant(kaolinite)	A_{11K}	1.67×10^{-19}	J
Hamaker constant(smectite)	A_{11S}	1.98×10^{-19}	J
Hamaker constant(water)	$A_{22water}$	3.7×10^{-20}	J
Permittivity of free space	ε_0	8.85×10^{-12}	$C^2J^2m^{-1}$
Relative dielectric constant of water	ε_r	76.58	/
Boltzmann constant	k_B	1.38×10^{-23}	J/K
Electron charge	e	1.6×10^{-19}	C
Ion valence	z	1	/
Temperature(30°C)	T	303	K
Characteristic decay length of water	λ	0.6–2	nm
Coefficient of structural force	K	$\sim 10^7$-10^8	N/m^2

$$R_{FW} = \begin{cases} 0 & if\ r < fp \\ \left(1 - \frac{fp}{r}\right)^2 & if\ r > fp \end{cases} \quad (14)$$

where R_{SBW}, R_{IBW}, R_{OBW}, and R_{FW} separately refer to the ratios of the SBW, IBW, OBW, and FW layers in certain-sized pores under saturated state. r is the pore radius of certain pore, nm. The sp, tp, and fp separately represent the lengths of shear plane, threshold plane and free plane, nm.

The ratio of SBW decreases with pore size and becomes minor when the diameter excesses 2tp, that of IBW increases with diameter when it < 2tp but decreases when diameter > 2tp, that of OBW shows a reversed trend when the size excesses 2fp, while that of FW increases with pore size since it appears, which dominates the water mobility in the pores with diameters > 20000 nm. The ratio of potential movable water (IBW + OBW + FW), representing the maximum static flow mobility in certain-sized pores, is positively correlated with the permeability, while the ratio of the immovable water (SBW) shows an opposite correlation (Table 7).

To characterize the dynamic variation of gas accessibility in the UTFF, the effective flow radius model is introduced, which can be described by the Eq. (15) (Carman, 1956; Civan, 2013; Wang et al., 2015). According to the connected flow pathway identified, the equation can be modified to the Eq. (16).

$$r_e = \sqrt{\frac{8\tau k_w}{\varphi}} \quad (15)$$

$$r_{ec} = \sqrt{\frac{8\tau_c k_w}{\varphi_c}} \quad (16)$$

where r_e is the effective flow radius, τ is the tortuosity, k_w is the water apparent permeability in the experiments,r_{ec} is the effective flow radius of the connected pore system, τ_c is the tortuosity of the connected pore system, φ_c is the porosity of the connected pore system.

According to the features of the UTFF, we make a reasonable assumption that the calculated effective flow radius equals to gas flow radius inside the cores under the equilibrium condition. By means of combining the water layer distribution and dynamic changes of effective flow radius, the dynamic gas accessibility can be de deduced (Fig. 16 A-D). Initially, gas intrudes into the pores with diameters > 3020 nm and occupies the FW zone when the applied pressure is far less than ISTP, leading to the water permeability fluctuations in the early stage. In this stage, no continuous water flow occurs, because whole pore systems are not interconnected under the blockage generated from the pores with sizes < 40 nm existing between them. In this procedure, the FW zones may be gradually fully occupied by gas (Fig. 16 A). When the applied injection pressure > ISTP, the water in IBW zone, particularly in the zone of pores < 40 nm, starts to move, where a connected gas flow pathway forms and an effective flow radius appears, leading to the continuous water flow in downstream (Fig. 16 B). The increasing effective flow radius indicates the enhancement in gas accessibility. The increments in the gas ratios in the pore system, describing the dynamic gas accessibility variations along with the increase of injection pressure, could be determined by integrating the water layer distribution, effective gas flow radius, and CFPSDs. The results are shown as histograms in Fig. 16 A-C. The gas storage capacity of tight porous sandstone is probably dominated by the FW ratios, while the gas accessibility increases happening in the continuous fluid flow procedure mainly originate from the water movement in the OBW zone since the water movement in IBW zone is volumetrically minor, however, the criticalities of gas accessibility increases are determined by the volumetrically minor IBW zone (Fig. 16). The samples with greater ISTPs are generally characterized by worse gas accessibility and lower accessibility increment in UTFF (Fig. 16).

Table 6
Distances from the solid surface to the shear plane (sp), threshold plane (tp), and free plane (fp).

Sample	sp, nm	tp, nm	fp, nm
1#	0.82	18.49	1509.97
3#	0.75	18.30	1509.97
6#	0.88	18.63	1509.97
8#	0.77	18.38	1509.97
12#	0.82	18.39	1509.97
15#	0.91	18.58	1509.97
19#	0.78	18.39	1509.97
25#	0.77	18.38	1509.97
26#	0.77	18.38	1509.97

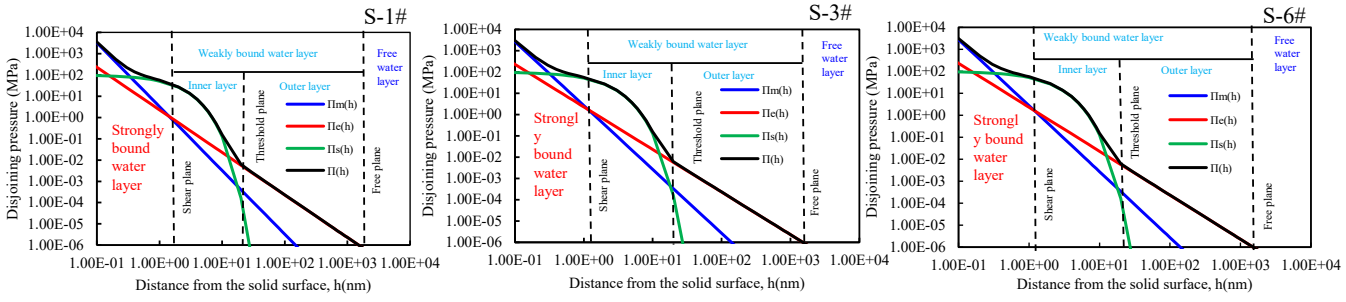

Fig. 14. The water layer distribution of three tight sandstone samples according to the variations of disjoining pressures along with the distances from the solid surface. The shear plane is the interface plane between the compact and diffuse layers in the electrical double layer model. The location of the shear plane approaches the plane where the electrostatic force equals molecular force. The threshold plane is the plane where the structural force equals molecular force. The free plane is the plane where the interfacial force is almost 0. sp, tp, and fp separately represent the distances from solid surface to shear plane, threshold plane, and free plane.

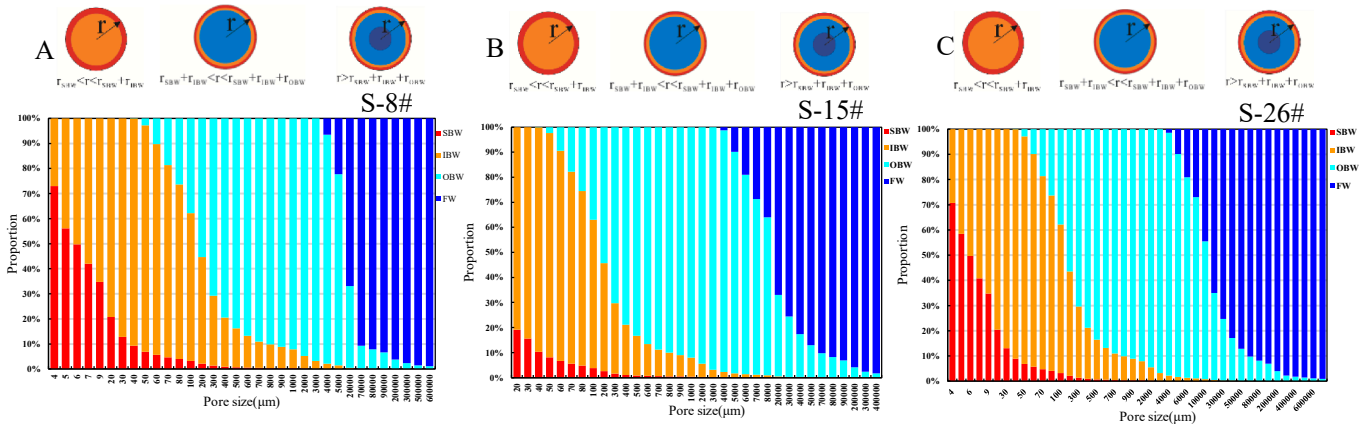

Fig. 15. Histograms displaying the static fluid mobility potential based the combination of the water layer distribution in certain-sized pores and CFPSD.

Table 7
Static fluid mobility and dynamic gas accessibility.

Sample	Ratio of SBW	Ratio of IBW	Ratio of OBW	Ratio of FW	Ratio of Potential movable water	Dynamic gas increment proportion, %
1#	0.0023	0.042	0.23	0.7257	0.99	15.58
3#	0.0373	0.33	0.39	0.2427	0.96	11.09
6#	0.0053	0.090	0.46	0.4447	0.99	24.35
8#	0.0043	0.066	0.69	0.2397	0.99	7.69
12#	0.0023	0.042	0.39	0.5657	0.99	23.17
15#	0.0058	0.082	0.45	0.4622	0.99	19.47
19#	0.014	0.14	0.46	0.3860	0.98	18.39
25#	0.012	0.19	0.68	0.1180	0.98	3.03
26#	0.0093	0.11	0.27	0.6107	0.99	12.39

Note that SBW, IBW, OBW, and FW separately refer to the strongly bound, inner layer of weakly bound, outer layer of weakly bound, and free water layers from the solid surface.

Under the ideal circular pore assumption, the movement, occurrence, and distribution of fluids would inevitably associated with the pore attributes, the situation presents a picture of extreme in tight porous sandstone with micro-nanometer scale pore structures. The ratio of immovable fluids, namely, the ratio of SBW, and ratios of potential movable fluids, the ratios of IBW and OBW, are negatively correlated with D_{c50}, while the movable fluid ratio, proportion of FW, shows a positive correlation with D_{c50}, suggesting the rises in the free fluid mobility with increasing pore sizes of the connected flow pathway (Fig. 17 A–D). This can be further supported by the negative correlation between the D_{c50} and sum proportion of SBW and IBW (zones where fluid can hardly flow) (Fig. 17 G), and the positive relationship between D_{c50} and sum proportion of OBW and FW (zones where fluid can easily flow) (Fig. 17 H). The heterogeneity exerts a relative poor effect on the fluid mobility, which has a positive correlation with ratio of OBW and a negative correlation with that of FW, indicating that the heterogeneity increase will lead to reductions in the static fluid mobility (Fig. 17 E, F). However, under the dynamic conditions, the dramatic decreases in the correlation coefficients suggest the effects of the pore size and heterogeneity reduce evidently (Fig. 18 A, B). The strong negative correlation between the τ_c and gas accessibility suggests the UTFF in the primary gas intrusion or charging processes are controlled by the pore size, complexity, and heterogeneity in couple (Fig. 18 C).

4. Conclusion

In this paper, an unsteady-state two-phase flow (UTFF) experiment is conducted on the natural tight sandstone to investigate the fluid flow in the primary CO_2 intrusion and natural gas charging processes. The fluid flow behaviors are investigated by experimental analyses combining

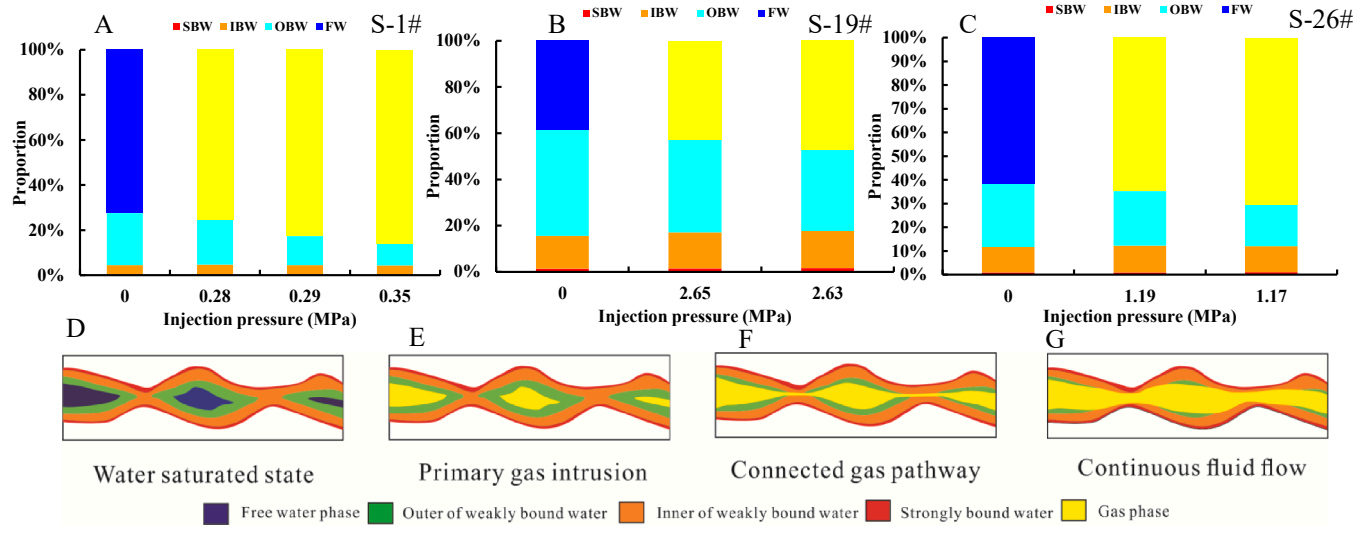

Fig. 16. Histograms displaying the dynamic gas accessibility in the UTFF in the primary gas intrusion procedure (A-C) and the sketch maps for the water layer distribution variations and dynamic gas accessibility in the procedure (D–F).

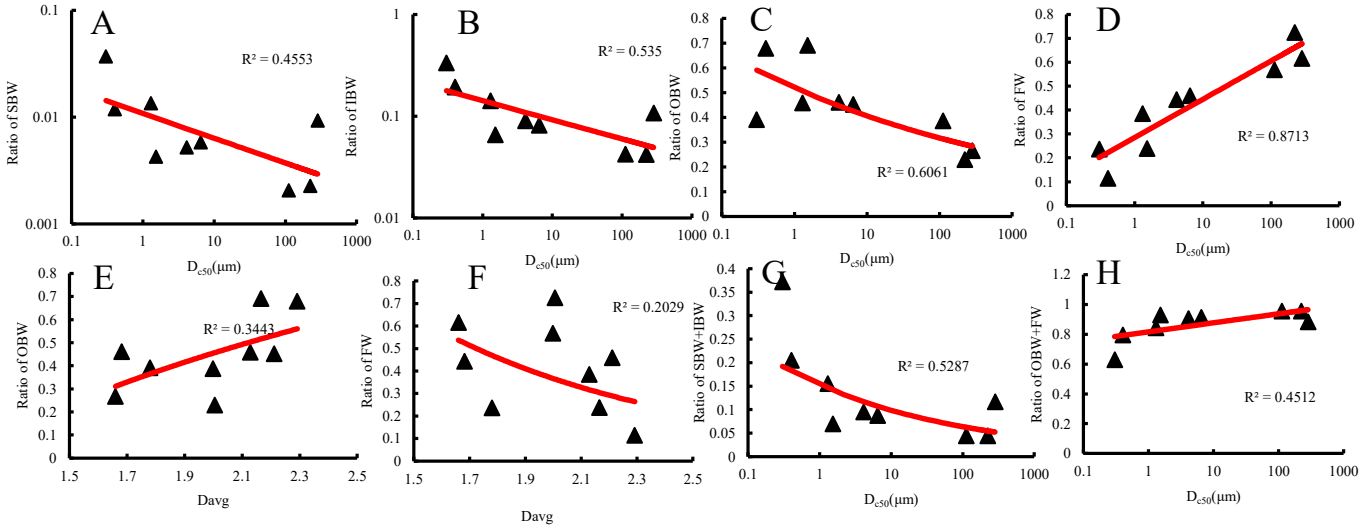

Fig. 17. Effects of D_{c50} and pore system heterogeneity (D_{avg}) on the static fluid mobility in the micro-nanometer pore system of the tight porous sandstone.

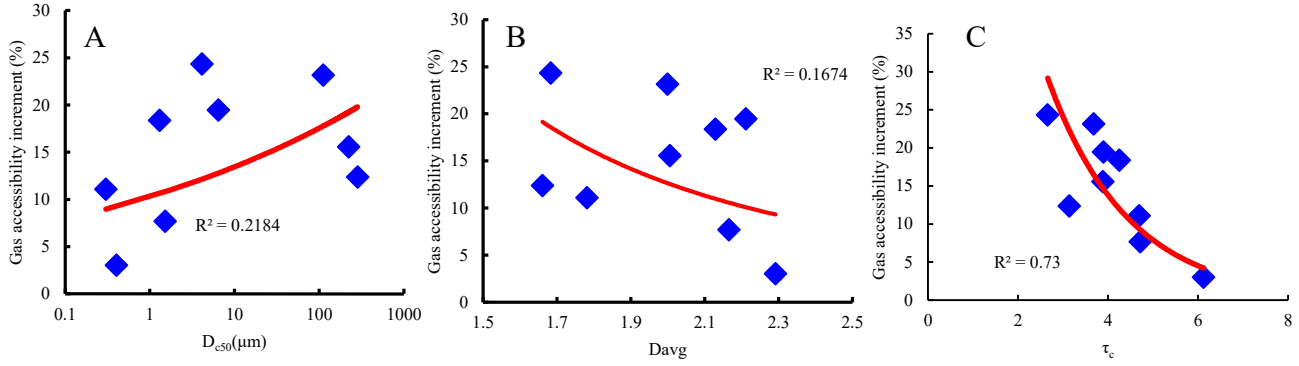

Fig. 18. Correlations between the D_{c50}, D_{avg}, τ_c, and dynamic gas accessibility increment in the UTFF.

water layer theory and effective flow radius model, and their pore-scale controls are discussed by the systematic pore structure characterization. The conclusions can be drawn as follow:

The UTFF in the primary gas intrusion or charging process is low-velocity non-linear flow with evident threshold for the onset of the continuous non-wetting phase fluid intrusion (ISTP), of which flow regime of the wetting phase fluid can be given as $v = \begin{cases} 0 & if \ \frac{dP}{dL} \le \frac{dP_0}{dL} \\ a\left(\frac{dP}{dL}\right)^m & if \ \frac{dP}{dL} \ge \frac{dP_0}{dL} \end{cases}$.

The connected pathways for fluid flow in tight sandstone are identified by an innovative pore connectivity evaluation combining NMR and X-μCT on the basis of systematic pore system characterization. The connected pore systems have wide pore size distributions (PSD) between 3.2 nm and 758.20 μm with connectivity dominated by the pores with diameters > 100 μm, and heterogeneous tri-fractal structures with average fractal dimension ranging from 1.66 to 2.29. The connected pore networks vary significantly in tight porous sandstone with minimum pore diameter between 3 and 129 nm, median pore diameter ranging from 302.5 nm to 283.3 μm, and maximum pore diameter in the range of 120.3–629.61 μm.

The static fluid mobility evaluation combining water layer theory and connected full-range PSD suggests high water mobility in the connected pathways, with the sum of proportions of free water layer and outer layer of weakly bound water in the range of 71.22–97.66%. The ISTPs are probably attributed to the presences of the pores < 40 nm in the connected pathways.

The dynamic gas accessibilities in the UTFF process are deduced by combining the circular pore assumption, effective flow radius variation, and water layer distribution under the equilibrium condition. Gas accessibility is dominated by the water movements in the free water layer zone when injection pressure < ISTP, while criticalities for its continuous increases are determined by the water movement in the inner layer of weakly bound water zone in the pores with sizes < 40 nm presented in the connected flow pathway but its dynamic increments mainly originate from the water movement in the outer layer of weakly bound water zone during the continuous two-phase fluid flow processes.

The complex structural attributes of connected pore system in the tight porous sandstone exert great impacts on the UTFF. The narrowing and heterogeneity and actual flow length increases of the connected pathways raise the flow resistances and lead to fluid velocity and gas accessibility losses in the UTFF. The differentiated connected pore systems are responsible for the flow behavior and capability differences among tight porous sandstone. The high sensitivities of the static fluid mobility and dynamic flow parameters to the tortuosity suggest that the UTFF flow behaviors are controlled by pore size, complexity, and heterogeneity in couple.

This study provides a deep understanding for the unsteady-state multiphase flow behaviors in the primary non-wetting phase fluid intrusion or charging procedure in the natural tight porous rocks and

their pore-scale controlling factors, which may enlighten the geologists and engineers when they are working on their own scene, especially the CO_2 geologic sequestration and exploration and development of the unconventional natural gas resources.

CRediT authorship contribution statement

Juncheng Qiao: Conceptualization, Methodology, Software, Investigation, Writing – original draft. **Jianhui Zeng:** Supervision, Writing – review & editing, Project administration, Funding acquisition, Resources. **Shu Jiang:** Investigation. **Guangqing Yang:** Software. **Yongchao Zhang:** Investigation. **Xiao Feng:** Software. **Sen Feng:** Investigation.

Declaration of Competing Interest

The authors declare that they have no known competing financial interests or personal relationships that could have appeared to influence the work reported in this paper.

Acknowledgements

This study is supported by the National Natural Science Foundation of China (Grant Nos. 41330319, 42130803, and 42072174), Foundation of China University of Petroleum Beijing (Grant No.2462020XKBH016), and Fellowship of China Postdoctoral Science Foundation (Grant No.2020M680030). We sincerely appreciate all anonymous reviewers and the handling editor for their comments and suggestions.

References

Armstrong, R.T., McClure, J.E., Berrill, M.A., Rücker, M., Schlüter, S., Berg, S., 2016. Beyond Darcy's law: The role of phase topology and ganglion dynamics for two-fluid flow. Phys. Rev. E 94 (04), 043113.
Bachu, S., 2000. Sequestration of CO_2 in geological media: Criteria and approach for site selection in response to climate change. Energy Convers. Manage. 41 (9), 953–970.
Bağcı, Ö., Dukhan, N., Özdemir, M., 2014. Flow regimes in packed beds of spheres from pre-Darcy to turbulent. Transport Porous Med. 104 (3), 501–520.
Bale, H.D., Schmidt, P.W., 1984. Small-angle X-ray scattering investigation of submicroscopic porosity with fractal properties. Phys. Rev. Lett. 53 (6), 596–599.
Berg, S., Ott, H., Klapp, S.A., Schwing, A., Neiteler, R., Brussee, N., Makurat, A., Leu, L., Enzmann, F., Schwarz, J.O., Kersten, M., Irvine, S., Stampanoni, M., 2013. Real-time 3D imaging of Haines jumps in porous media flow. P. Natl. A. Sci. 110 (10), 3755–3759.
Bickle, M.J., 2009. Geological carbon storage. Nat. Geosci. 2 (12), 815–818.
Blunt, M.J., 2017. Multiphase Flow in Permeable Media: A Pore-Scale Perspective. Cambridge University Press, London.
Bultreys, T., De Boever, W., Cnudde, V., 2016. Imaging and image-based fluid transport modeling at the pore scale in geological materials: A practical introduction to the current state-of-the-art. Earth-Sci. Rev. 155, 93–128.
Carman, P.C., 1956. Flow of Gases Through Porous Media. Academic Press, New York.
Chen, Y., Lian, H., Liang, W., Yang, J., Nguyen, V.P., Bordas, S.P., 2019. The influence of fracture geometry variation on non-Darcy flow in fractures under confining stresses. Int. J. Rock Mech. Min. Sci. 113, 59–71.
Chhabra, R.P., 2006. Bubbles, drops, and particles in non-Newtonian Fluids. CRC Press, Boca Raton.
Churaev, N., 2003. Surface forces in wetting films. Colloid J+. 65 (3), 263–274.
Civan, F., 2013. Modeling gas flow through hydraulically-fractured shale-gas reservoirs involving molecular-to-inertial transport regimes and threshold-pressure gradient, Paper presented at the SPE annual technical conference and exhibition (SPE 166324), New Orleans, LA.
Comiti, J., Sabiri, N., Montillet, A., 2000. Experimental characterization of flow regimes in various porous media: 3: Limit of Darcy's or creeping flow regime for Newtonian and purely viscous non-Newtonian fluids. Chem. Eng. Sci. 55 (15), 3057–3061.
Dai, J., Li, J., Luo, X., Zhang, W., Hu, G., Ma, C., Guo, J., Ge, S., 2005. Stable carbon isotope compositions and source rock geochemistry of the giant gas accumulations in the Ordos Basin. China. Org. Geochem. 36 (12), 1617–1635.
Darcy, H., 1856. Les Fontaines Publiques de la ville de Dijon: Exposition et Application. Victor Dalmont, Paris.
Dejam, M., Hassanzadeh, H., Chen, Z., 2017a. Pre-Darcy flow in Tight and Shale Formations. Bull. Am. Phys. Soc. 62.
Dejam, M., Hassanzadeh, H., Chen, Z., 2017b. Pre-Darcy Flow in Tight and Shale Formations. APS Search 53 (10), 8187–8210.
Dong, H., Blunt, M.J., 2009. Pore-network extraction from micro-computerized-tomography images. Phys. Rev. E 80 (3), 036307. https://doi.org/10.1103/PhysRevE.80.036307.
Dou, H.E., Ma, S.Y., Zou, C.Y., Yao, S.L., 2014. Threshold pressure gradient of fluid flow through multi-porous media in low and extra-low permeability reservoirs. Sci. China Earth Sci. 57 (11), 2808–2818.
Dukhan, N., Bağcı, Ö., Özdemir, M., 2014. Metal foam hydrodynamics: flow regimes from pre-Darcy to turbulent. Int. J. Heat Mass Trans. 77, 114–123.
Durlofsky, L., Brady, J., 1987. Analysis of the Brinkman equation as a model for flow in porous media. Phys Fluid. 30 (11), 3329–3341.
Farmani, Z., Azin, R., Fatehi, R., Escrochi, M., 2018. Analysis of pre-darcy flow for different liquids and gases. J. Petrol. Sci. Eng. 168, 17–31.
Gavin, L., 2004. Pre-Darcy flow: a missing piece of the improved oil recovery puzzle?, Paper presented at the SPE/DOE symposium on improved oil recovery, Tulsa, Oklahoma.
Haines, W.B., 1930. Studies in the physical properties of soil. V. The hysteresis effect in capillary properties, and the modes of moisture distribution associated therewith. J. Agric. Sci. 20 (1), 97–116.
Hansbo, S., 2001. Consolidation equation valid for both Darcian and non-Darcian flow. Geotechnique 51 (1), 51–54.
Hui, W., Wang, Y.S., Ren, D.Z., Jin, H., 2020. Effects of pore structures on the movable fluid saturation in tight sandstones: A He8 formation example in Sulige Gasfield, Ordos Basin, China. J. Petrol. Sci. Eng. 192, 107295 (in press).
Israelachvili, J.N., 2015. Intermolecular and surface forces. Academic press, London, UK.
Javadpour, F., 2009. Nanopores and apparent permeability of gas flow in mudrocks (shales and siltstone). J. Can. Petrol. Technol. 48 (08), 16–21.
Kececioglu, I., Jiang, Y., 1994. Flow through porous media of packed spheres saturated with water. J. Fluids Eng. 116 (1), 164–170.
Kleinberg, R.L., 1996. Utility of NMR T_2 distributions, connection with capillary pressure, clay effect, and determination of the surface relaxivity parameter ρ2. Magn. Reson. Imaging 14 (7–8), 761–767.
Kundu, P., Kumar, V., Mishra, I.M., 2016. Experimental and numerical investigation of fluid flow hydrodynamics in porous media: characterization of pre-Darcy, Darcy and non-Darcy flow regimes. Powder Technol. 303, 278–291.
Kutilek, M., 1972. Non-darcian flow of water in soils-laminar region: A review. Dev. Soil Sci. 2, 327–340.
Lai, J., Wang, G., Fan, Z., Zhou, Z., Chen, J., Wang, S., 2018a. Fractal analysis of tight shaly sandstones using nuclear magnetic resonance measurements. AAPG Bull. 102 (02), 175–193.
Lai, J., Wang, G., Wang, Z., Chen, J., Pang, X., Wang, S., Zhou, Z., He, Z., Qin, Z., Fan, X., 2018b. A review on pore structure characterization in tight sandstones. Earth-Science Rev. 177, 436–457.
Lebeau, M., Konrad, J.M., 2010. A new capillary and thin film flow model for predicting the hydraulic conductivity of unsaturated porous media. Water Res. Res. 46 (12) https://doi.org/10.1029/2010WR009092.
Li, K., Horne, R.N., 2006. Fractal modeling of capillary pressure curves for The Geysers rocks. Geothermics 35 (2), 198–207.
Liu, Y., Dong, X., Chen, Z., Hou, Y., Luo, Q., Chen, Y., 2021. A novel experimental investigation on the occurrence state of fluids in microscale pores of tight reservoirs. J. Petrol. Sci. Eng. 196, 107656. https://doi.org/10.1016/j.petrol.2020.107656.
Loucks, R.G., Reed, R.M., Ruppel, S.C., Jarvie, D.M., 2009. Morphology, genesis, and distribution of nanometer-scale pores in siliceous mudstones of the Mississippian Barnett Shale. J. Sediment. Res. 79 (12), 848–861.
Mandelbrot, B.B., 1975. Les Objets Fractals: Forme, Hasard et Dimension. Flammarion, Paris.
Mandelbrot, B.B., Passoja, D.E., Paullay, A.J., 1984. Fractal character of fracture surfaces of metals. Nature 308 (5961), 721–722.
Miller, R.J., Low, P.F., 1963. Threshold gradient for water flow in clay systems. Soil Sci. Soc. Am. J. 27 (6), 605–609.
Mohnke, O., 2014. Jointly deriving NMR surface relaxivity and pore size distributions by NMR relaxation experiments on partially desaturated rocks. Water Resour. Res. 50 (6), 5309–5321.
Muljadi, B.P., Blunt, M.J., Raeini, A.Q., Bijeljic, B., 2016. The impact of porous media heterogeneity on non-Darcy flow behaviour from pore-scale simulation. Adv. Water Resour. 95, 329–340.
Nelson, P.H., 2009. Pore-throat sizes in sandstones, tight sandstones, and shales. AAPG Bull. 93 (3), 329–340.
Pascal, H., 1981. Nonsteady flow through porous media in the presence of a threshold gradientInstationre Strmung durch porse Medien bei Vorhandensein eines Schwellgradienten. Acta Mech. 39 (3-4), 207–224.
Pertsin, A., Grunze, M., 2004. Water−graphite interaction and behavior of water near the graphite surface. J. Phys. Chem. B 108 (4), 1357–1364.
Prada, A., Civan, F., 1999. Modification of Darcy's law for the threshold pressure gradient. J. Petrol. Sci. Eng. 22 (4), 237–240.
Puzyrevskaya, T., 1931. Prosatchivanije vody tcherez pestchanye grunty. Izuestiya NIIG.
Qiao, J., Zeng, J., Cai, J., Jiang, S., An, T., Xiao, E., Zhang, Y., Feng, X., Yang, G., 2021. Pore-scale heterogeneity of tight gas sandstone: Origins and impacts. J. Nat. Gas Sci. Eng. 96, 104248. https://doi.org/10.1016/j.jngse.2021.104248.
Qiao, J., Zeng, J., Jiang, S., Feng, S., Feng, X., Guo, Z., Teng, J., 2019. Heterogeneity of reservoir quality and gas accumulation in tight sandstone reservoirs revealed by pore structure characterization and physical simulation. Fuel 253, 1300–1316.
Qiao, J., Zeng, J., Jiang, S., Wang, Y., 2020a. Impacts of sedimentology and diagenesis on pore structure and reservoir quality in tight oil sandstone reservoirs: Implications for macroscopic and microscopic heterogeneities. Mar. Petrol. Geol. 111, 279–300.
Qiao, J., Zeng, J., Jiang, S., Zhang, Y., Feng, S., Feng, X., Hu, H., 2020b. Insights into the pore structure and implications for fluid flow capacity of tight gas sandstone: A case study in the upper paleozoic of the Ordos Basin. Mar. Petrol. Geol. 118, 104439. https://doi.org/10.1016/j.marpetgeo.2020.104439.

Ramstad, T., Øren, P.E., Bakke, S., 2010. Simulation of two-phase flow in reservoir rocks using a lattice Boltzmann method. SPE J. 15 (04), 917–927.
Siddiqui, F., Soliman, M.Y., House, W., Ibragimov, A., 2016. Pre-Darcy flow revisited under experimental investigation. J. Anal. Sci. Technol. 7 (01), 1–9.
Singh, H., Javadpour, F., Ettehadtavakkol, A., Darabi, H., 2014. Nonempirical apparent permeability of shale. SPE Reserv. Eval. Eng. 17 (03), 414–424.
Singh, K., Menke, H., Andrew, M., Lin, Q., Rau, C., Blunt, M.J., Bijeljic, B., 2017. Dynamics of snap-off and pore-filling events during two-phase fluid flow in permeable media. Sci. Rep. 7 (1) https://doi.org/10.1038/s41598-017-05204-4.
Slepicka, F., 1961. The laws of filtration and limits of their validity. In: IAHR Proceedings 9th Convention, pp. 383–394.
Soni, J.P., Islam, N., Basak, P., 1978. An experimental evaluation of non-Darcian flow in porous media. J. Hydrol. 38 (3-4), 231–241.
Spurin, C., Bultreys T., Rücker M., Garfi G., Schlepütz C., Novak V., Berg S., Blunt M., Krevor, S., 2020. Real-time imaging reveals distinct pore scale dynamics during transient and equilibrium subsurface multiphase flow. Water Resour. Res., 56(12): e2020WR028287.
Swartzendruber, D., 1962a. Modification of Darcy's law for the flow of water in soils. Soil Sci. 93 (01), 22–29.
Swartzendruber, D., 1962b. Non-Darcy flow behavior in liquid-saturated porous media. J. Geophys. Res. 67 (13), 5205–5213.
Tallakstad, K.T., Knudesen, H.A., Ramstad, T., Løvoll, G., Måløy, K.J., Toussaint, R., Flekkøy, E., 2009a. Steady-state two-phase flow in porous media: statistics and transport properties. Phys. Rev. Lett. 102 (07), 074502.
Tallakstad, K.T., Løvoll, G., Knudesen, H.A., Ramstad, T., Flekkøy, E., Måløy, K.J., 2009b. Steady-state, simultaneous two-phase flow in porous media: An experimental study. Phys. Rev. E 80 (03), 036308.
Thomas, R.D., Ward, D.C., 1972. Effect of overburden pressure and water saturation on gas permeability of tight sandstone cores. J. Petrol. Technol. 24 (02), 120–124.
Tischner, T., et al., 2010. New concepts for extracting geothermal energy from one well: the GeneSys-Project. In: Proceedings of the world geothermal congress.
Torrey, H.C., 1956. Bloch equations with diffusion terms. Phys. Rev. 104 (3), 563–565.
Tuller, M., Or, D., 2003. Hydraulic functions for swelling soils: Pore scale considerations. J. Hydrol. 272 (1–4), 50–71.
Wang, J., Liu, H., Wang, L., Zhang, H., Luo, H., Gao, Y., 2015. Apparent permeability for gas transport in nanopores of organic shale reservoirs including multiple effects. Int. J. Coal Geol. 152, 50–62.
Wang, X., Sheng, J.J., 2017. Effect of low-velocity non-Darcy flow on well production performance in shale and tight oil reservoirs. Fuel 190, 41–46.
Woodruff, W., Revil, A., 2011. CEC-normalized clay-water sorption isotherm. Water Resour. Res. 47 (11), W11502.
Wu, J., Cheng, L., Li, C., Cao, R., Chen, C., Cao, M., Xu, Z., 2017a. Experimental study of nonlinear flow in micropores under low pressure gradient. Transport Porous Med. 119 (1), 247–265.
Wu, K., Chen, Z., Li, J., Li, X., Xu, J., Dong, X., 2017b. Wettability effect on nanoconfined water flow. Proc. Natl. Acad. Sci. 114 (13), 3358–3363.
Xia, C.C., Qian, X., Lin, P., Xiao, W.M., Gui, Y., 2017. Experimental investigation of nonlinear flow characteristics of real rock joints under different contact conditions. J. Hydraul. Eng. 143 (3), 04016090. https://doi.org/10.1061/(ASCE)HY.1943-7900.0001238.
Xiao, D., Lu, S., Yang, J., Zhang, L., Li, B., 2017. Classifying multiscale pores and investigating their relationship with porosity and permeability in tight sandstone gas reservoirs. Energy Fuel. 31 (9), 9188–9200.
Xiao, X.M., Zhao, B.Q., Thu, Z.L., Song, Z.G., Wilkins, R.W.T., 2005. Upper Paleozoic petroleum system, Ordos Basin. China. Mar. Petrol. Geol. 22 (8), 945–963.
Yang, S., Yu, Q., 2020. Experimental Investigation on the Movability of Water in Shale Nanopores: A case study of carboniferous chale from the Qaidam Basin, China. Water Resour. Res. 56 (08) e2019WR026973.
Yang, Y., Li, W., Ma, L., 2005. Tectonic and stratigraphic controls of hydrocarbon systems in the Ordos basin: A multicycle cratonic basin in central China. AAPG Bull. 89 (2), 255–269.
Zeng, J., Cheng, S., Kong, X., Guo, K., Wang, H., 2010. Non-Darcy flow in oil accumulation (oil displacing water) and relative permeability and oil saturation characteristics of low-permeability sandstones. Petrol. Sci. 7 (1), 20–30.
Zeng, Z., Grigg, R., 2006. A criterion for non-Darcy flow in porous media. Transport. Porous Med. 63 (1), 57–69.
Zhang, Y., Zeng, J., Qiao, J., Feng, X., Wang, F., Ren, N., 2016. Experimental study on natural gas migration and accumulation mechanism in sweet spots of tight sandstones. J. Nat. Gas Sci. Eng. 36, 669–678.
Zou, L., Jing, L., Cvetkovic, V., 2017. Shear-enhanced nonlinear flow in rough-walled rock fractures. Int. J. Rock Mechan. Min. Sci. 97, 33–45.